ELSEVIER

Tectonophysics 263 (1996) 191–218

TECTONOPHYSICS

Heat flow in the Alboran Sea, western Mediterranean

B.G. Polyak [a], M. Fernàndez [b,*], M.D. Khutorskoy [c], J.I. Soto [d], I.A. Basov [e], M.C. Comas [d], V.Ye. Khain [e], B. Alonso [g], G.V. Agapova [a], I.S. Mazurova [f], A. Negredo [b], V.O. Tochitsky [c], J. de la Linde [d], N.A. Bogdanov [e], E. Banda [b]

[a] *Geological Institute, Russian Academy of Sciences, Pyzhevsky per., 7, 109017 Moscow, Russia*
[b] *Institute of Earth Sciences (J. Almera), CSIC, Martí i Franqués s / n. 08028, Barcelona, Spain*
[c] *Russian University of Peoples Friendship, Miklukho-Maklay str., 19, 117198 Moscow, Russia*
[d] *Instituto Andaluz de Geología Mediterránea, CSIC, Universidad de Granada, Campus de Fuentenueva s / n, 18002 Granada, Spain*
[e] *Institute of Lithosphere, Russian Academy of Sciences, Staromonetny per., 22, 109180 Moscow, Russia*
[f] *Scientific-Industrial State Association "Neftegeofizika", Chernyshevskogo str., 22, 101000 Moscow, Russia*
[g] *Instituto de Ciencias del Mar, CSIC, Paseo Juan de Borbón s / n, 08039 Barcelona, Spain*

Received 1 February 1995; accepted 1 November 1995

Abstract

The results of the first regional heat flow survey carried out in the Alboran Basin are presented. The survey consists of 98 heat flow measurements obtained using a violin type probe, 697 nautic miles of gravity profiles, 1446 nautic miles of bathymetric survey, and 22 gravity cores. A remarkable difference in heat flow patterns exists between the western (WAB) and eastern (EAB) parts of the Alboran Basin. The average heat flow in the WAB is 69 ± 6 mW m^{-2} with a generally increasing trend towards the centre and to the east. In contrast, the heat flow pattern in the EAB shows an average value of 124 ± 8 mW m^{-2} and it is maintained rather constant for the overall area. Superimposed on this general pattern there are some local thermal anomalies, associated with hydrothermal activity, which have been detected in the central WAB (up to 123 mW m^{-2}), in the South Alboran Basin (SAB) (up to 153 mW m^{-2}) and in the Djibouti Bank (DB) (up to 254 mW m^{-2}). After corrections for thermal refraction, sedimentation and cooling of volcanic bodies, the resulting heat flow distribution in the WAB is smoother, but still shows the increasing trend towards the centre and to the east. In the EAB, the application of these corrections did not lead to any noticeable changes. A 1-D approach that combines heat flow data, crustal structure and elevation shows a dramatic decrease in lithospheric thickness from the WAB (50–90 km) to the EAB (38–40 km). Likewise, the resulting crustal thickness is around 14–16 km in the central part of the WAB, increasing towards the borders of the basin, whereas in the EAB the crustal thickness varies between 12.5 and 14.5 km in its western part, and between 10 and 11.5 km in its eastern part.

1. Introduction

The Alboran Sea has been identified as one of the main targets to address geophysical investigations on present-day crustal deformation and lithospheric behaviour in extensional basins developed in collisional settings at convergent plate boundaries. A consensus generally exists recognizing the importance of this land-locked westernmost Mediterranean basin for the understanding of the origin and geodynamic evolution of the whole Mediterranean Sea.

* Corresponding author. Fax: 34-3-4110012. E-mail: mfernandez@u.ija.csic.es.

0040-1951/96/$15.00 Published by Elsevier Science B.V.
SSDI 0040-1951(95)00178-6

The Alboran Sea Basin has been the site of a vigorous program of oil and gas exploration since the early 1970's. As a result, a dense network of commercial seismic reflection profiles is now available. Several scientific surveys have been carried out in the Alboran Sea since 1988, mostly by Spanish, British and American groups: single channel seismic profiles, deep seismic reflection profiles (up to 20 s twtt), magnetic, gravity, multibeam bathymetry and side-scan sonar surveys. These data are complementary to those obtained in previous geophysical surveys (Allan and Morelli, 1971; Bonini et al., 1973; Hatzfeld, 1976; Hatzfeld et al., 1978).

The downhole information consists of data from DSDP Site 121 (Ryan et al., 1973) and five commercial wells: Andalucia G-1, Alboran A-1 and Andalucia A-1 (located on the Spanish side), and El Jebha-1 and Nador-1 (on the Moroccan side) (Fig. 1). Some of these commercial wells reached the metamorphic basement (Jurado and Comas, 1992).

Only three sea floor heat flow measurements were made previously in the Alboran Sea (Fig. 1; Haenel, 1979). Two of these measurements are located in the Western Alboran Basin, yielding values of 52 and 93 $mW\,m^{-2}$, respectively. The third measurement, in the central part of the Eastern Alboran Basin, resulted in a value of 33 $mW\,m^{-2}$. Following the approach of Albert-Beltran (1979) for onshore wells and considering the same bulk thermal conductivity (2.1 $W\,m^{-1}\,K^{-1}$) for offshore commercial wells, one could expect an eastward increase in heat flow values from 40 to 100 $mW\,m^{-2}$ on the Spanish shelf.

Different geodynamic hypotheses have been proposed to explain the origin and evolution of the Alboran Sea Basin. It has been considered as being either a subduction-related back-arc basin (Dercourt et al., 1986); a Mediterranean-type back-arc basin (Horvath and Berckhemer, 1982); a basin related to a mantle diapir (Weijermars, 1985); a basin related to

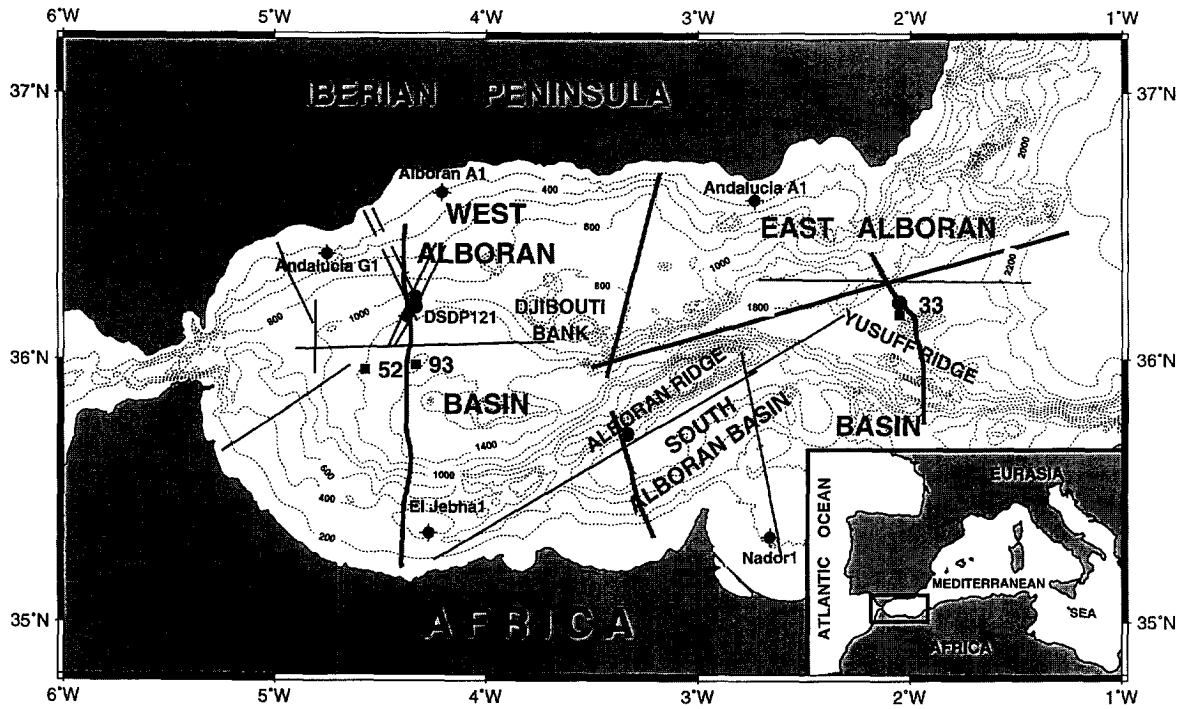

Fig. 1. Location of seismic reflection profiles and oil wells used in the FLUCALB (Flujo de Calor en Alboran) survey. Thick solid lines correspond to deep seismic data and thin solid lines correspond to commercial lines. ■ indicate previous heat flow measurements ($mW\,m^{-2}$) by Haenel (1979), ● indicate commercial oil wells and shaded circles indicate proposed ODP sites. Contour interval for bathymetry is 200 m.

convective removal of lithospheric root beneath a previous overthickenned crust (Platt and Vissers, 1989); or a basin related to an asymmetric delamination of the lithospheric mantle (Channel and Mareschal, 1989; García-Dueñas et al., 1992; Comas et al., 1993). Up to now, however, none of these models was able to explain successfully the observed pattern in geological and geophysical data. Surface heat flow data are an important information to test the validity of these competing genetic hypotheses.

In this context, a geological and geophysical project "FLUCALB" (Flujo de Calor en Alborán) was carried out in October 1993. The main goal of the project was to measure and obtain the regional variability in heat flow across the entire Alboran Basin. The FLUCALB survey was conducted during the 17th cruise of the Russian R/V "Akademik Nikolaj Strakhov". the cruise was organized in accordance with the World Ocean Program of the Russian Academy of Sciences within the frame of Russian–Spanish cooperation supported by the Russian Academy of Sciences (R.A.S.) and the "Consejo Superior de Investigaciones Científicas" (C.S.I.C.).

The FLUCALB programme included: (1) geothermal research, to measure temperature gradient in bottom sediments, thermal conductivity, heat flow density and bottom water temperature; (2) gravity survey and (3) bathymetry survey along previously selected profiles including the heat flow sites; and (4) study of lithological, paleontological and petrological characters of sediments recovered from gravity cores. In this paper we present preliminary results of this survey, mainly focusing on the heat flow and thermal structure of the Alboran Sea.

2. Geological and geophysical setting

The Alboran Sea, which is about 400 km long and 200 km wide, forms the westernmost part of the Mediterranean (Fig. 2). It is surrounded by an arcuate thrust belt (the Betic and Rifean chains) and the Gibraltar Arc, which was active before and during the extensional stages in basin evolution. The Alboran Sea Basin is formed in an overall convergent environment between the African and the Eurasian plates from mid-Oligocene to Recent times (Dewey et al., 1989). This convergent history is not directly reflected in the kinematics of either the Betic and Rifean chains, or in the extension in the Alboran Basin. The system as a whole is bounded to the north and south by the Iberian and African continental forelands, and to the west and east by the Atlantic Ocean and the oceanic Algerian–South Balearic Basin, respectively (Galdeano and Rossignol, 1977; Morelli, 1985).

The Alboran Crustal Domain (Internal Zones) (Fig. 2) of the surrounding Betic and Rif mountain chains represents the disrupted and extended fragments of a former convergent orogenic belt that evolved from the Late Cretaceous to the Early Miocene. Pre-Miocene convergence caused substantial crustal thickening accompanied by high-pressure/low-temperature metamorphism. The remains of this orogen affected by Miocene extension probably underlie much of the Alboran Sea. On-shore, extensional detachment systems and fault-bounded sedimentary basins of Miocene age are superimposed upon the continental collision structures. This extensional phase was accompanied by a distinctive low-pressure/high-temperature metamorphism, and it is responsible for the crustal thinning observed in the region (Platt and Vissers, 1989; García-Dueñas et al., 1992). Coeval with this extension, the collisional front migrated to the west producing crustal shortening in both the Iberian and Magrebian continental margins, and the Flysch Trough Units (Betic–Rifean external zones) (Balanyá and García-Dueñas, 1987; Comas et al., 1992; García-Dueñas et al., 1992).

The Alboran Sea has a rough bathymetry (Fig. 1) with several subbasins, ridges and banks, and is flanked by a narrow shelf, slope and rise topography. The Alboran Ridge is locally emergent at the Alboran Island and, like most of the residual banks, is formed by volcanic rocks. Seismic and well data show thick sedimentary sequences (up to 6–7 km), Early Miocene to Recent in age, filling graben or half-graben between basement highs in the Western Alboran Basin. The lower seismostratigraphic units, late Aquitanian–Burdigalian and Langhian–Serravallian in age correspond to olistostromes and overpressured claystone, respectively, which conditioned mud diapir provinces (Jurado and Comas, 1992). Marine Miocene sequences, lithostratigraphically similar to those of the Alboran Basin infill, crop out onshore in the Betics and Rif. This feature indicates that during

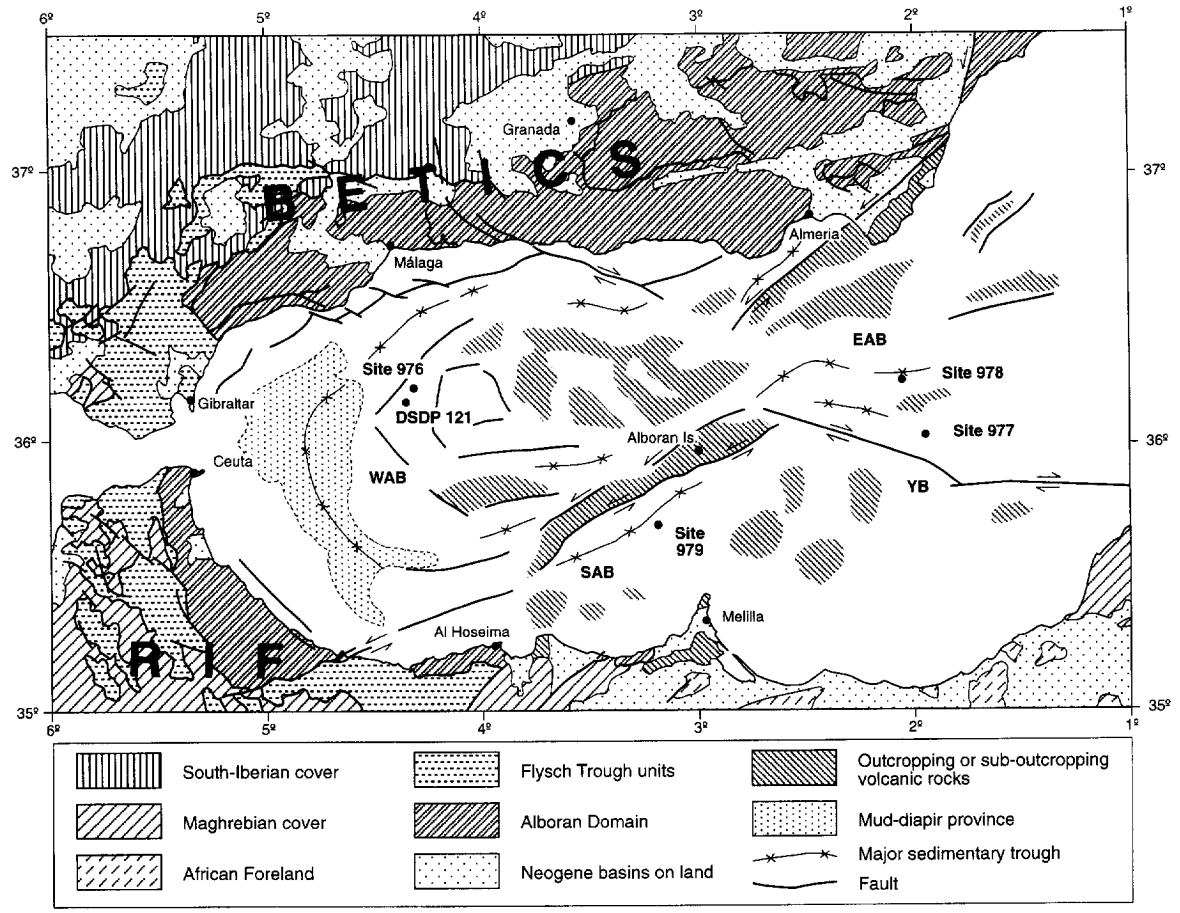

Fig. 2. Geological sketch map of the Alboran Basin and surrounding mountain chains. Modified from Comas et al. (1992, 1993). *WAB* = West Alboran Basin; *EAB* = East Alboran Basin; *SAB* = South Alboran Basin; *YB* = Yusuff Basin. Sites correspond to the 1995's Ocean Drilling Program proposal.

the Miocene the Alboran Basin occupied an area that extended both north and south beyond the present-day limits of the Alboran Sea. Seismic reflection data show that the sedimentary thickness reduces substantially in the Eastern Alboran Basin, where it reaches values around 1.5 km.

The basement of the Alboran Sea consists of rocks belonging to the metamorphic complexes that form the Alboran Crustal Domain, and outcrops in the Betic and Rif chains. Volcanoclastic and volcanic interbedding have been sampled in some of the exploration wells. Aeromagnetic anomalies indicate a pattern of volcanic ridges within the basin (Galdeano and Rossignol, 1977). These volcanic rocks can be correlated with alkaline and calc-alkaline rocks exposed onshore, late Serravallian–Early Pliocene in age (Hernandez et al., 1987; Comas et al., 1992).

The present-day configuration of the Alboran Basin is the result of the superimposition of different tectonic stages. Earlier structures correspond to extensional grabens generated through several rifting episodes and developed from the late Aquitanian (22 Ma) to the middle Tortonian (9 Ma). Magmatic events and mud diapirism were related to the extensional processes. The tectonic pattern was different for each extensional episode. First stages of crustal stretching which led to the Aquitanian transgression are not well recognized from seismic data; however, two episodes of main rifting with differing extension

directions, the Burdigalian–Langhian (about 17–15 Ma) and the Serravalian–early Tortonian (about 14–10 Ma), can be well stated (Comas et al., 1993). As a whole, directions of extension and rifting episodes recognized offshore are congruent with those recognized onshore for extensional systems that affect the metamorphic complexes in the emergent Alboran basement. Later structures (since about 7 Ma onwards) testify to a post-rift roughly N–S-oriented contraction, involving tectonic inversions, folding and strike-slip faulting. Latest tectonic organization, which conditioned the recent topography, occurred in the Pliocene–Quaternary during the Alboran Sea general subsidence (Comas et al., 1992).

Seismic refraction data, together with gravity modelling, show that the crust thins from about 38 km beneath the internal zones of the Betic and the Rif mountains, to about 15–20 km beneath the Alboran Sea (Hatzfeld, 1976; Hatzfeld et al., 1978; Banda and Ansorge, 1980; Torné and Banda, 1992; Watts et al., 1993). These data indicate that considerable thinning happened on a crust that was thickened during previous collisional stacking. Offshore crustal thinning can be related to large-scale extensional detachment faults recognized in the Betic and Rif chains (García-Dueñas et al., 1992). The seismic data are not complete enough to define the nature of the transition between Iberia, Africa and the Alboran Sea. Torné and Banda (1992) propose, based on gravity modelling, that the crustal thinning in the central part of the Alboran Basin occurs over a zone 30 km wide and exhibits a transform style, whereas in the eastern part the crust thins over an area 100 km wide, resembling the attitude of a rifted passive margin. Upper mantle velocities beneath the Betics are in the range of 8.1–8.2 km/s, whereas beneath the Alboran Sea they are characterized by lower values of 7.6–7.8 km/s (e.g., Hatzfeld, 1976; Banda and Ansorge, 1980).

3. Heat flow measurement technique

3.1. Survey location

Heat flow trajects were planned along available seismic reflection lines. This provides a good knowledge of the subbottom geological structure which is necessary for further interpretation of the acquired heat flow data. Additional heat flow measurements were made to coincide with Ocean Drilling Program (ODP) sites planned for 1995 and around some local thermal anomalies revealed during the cruise.

In addition to the thermal measurements, a bathymetric survey (1446 nautic miles total length), using both multi-beam and deep water echo sounders, and a gravity survey (697 nautic miles total length) were conducted along the selected heat flow trajects. Finally, bottom sediment sampling with gravity cores was performed at 22 sites in order to obtain detailed information of the lithological composition and porosity of the uppermost sediments. The geographical distribution of the heat flow measurements and gravity core sites, and the bathymetry and gravity surveys are shown in Fig. 3.

3.2. Measurement equipment

Heat flow measurements were carried out by means of a modified violin-type probe "GEOS-3M", a prototype of which was used during earlier cruises of the R/V "Akademik Nikolaj Strakhov" (Khutorskoy et al., 1990; Polyak et al., 1992). A detailed technical description of this probe is given in Matveev and Rot (1988). Essentially, the submersible unit of the GEOS-3M system consists of two measuring lines 2.0 m long (G-line and K-line), and a waterproof container (Fig. 4).

The "G-line", which measures the subbottom temperature and its gradient, includes five thermistors (temperature-sensitive resistors) placed along it at 0.5 m intervals. The lowest thermistor measures the absolute temperature with an accuracy of ± 5 mK at a depth of 2.0 m ($T_{2.0}$) when the probe fully penetrates into the sediments. The other four sensors measure the temperature differences between any of these sensors and the lowest one and, consequently, the temperature gradient at each 0.5 m interval. The absolute temperatures of these sensors ($T_{1.5}$, $T_{1.0}$, $T_{0.5}$ and $T_{0.0}$) are referred to the deepest sensor. The sensitivity of each thermistor and the accuracy in determining the geothermal gradient are ± 0.5 mK and ± 2 mK/m, respectively.

The "K-line" measures the thermal conductivity of sediments and is based on the needle probe technique (Von Herzen and Maxwell, 1959). It consists

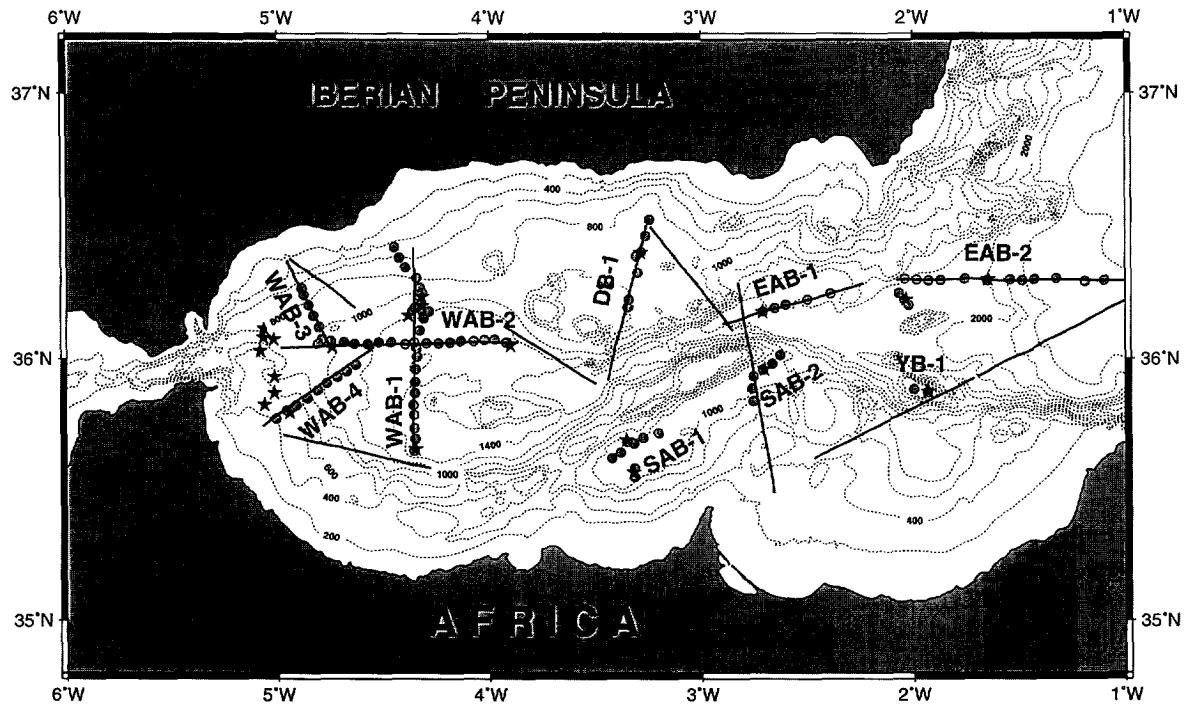

Fig. 3. Location of the sites of heat flow measurements (shaded circles), gravity cores (★), and gravity and bathymetry profiles (solid lines) carried out in the FLUCALB survey. Legends (*WAB-1*, *WAB-2*, etc.) correspond to the different heat flow trajects in Table 1Table 2.

of four independent heating elements with a length of 0.5 m each one, and four thermistors placed in the middle of each heater (Fig. 4). The thermal conductivity is determined at the mid-point of temperature measurements with an accuracy of 5%.

The container incorporates the electronics, and inclinometer to estimate the deviation of the probe from vertical position with an accuracy of $\pm 1°$, an independent temperature sensor to measure the absolute bottom water temperature with an accuracy of ± 2 mK, and a pressure gauge which allows to determine the water depth with an error of ± 1 m. The data recorded by all sensors were converted to digital code and polled to the on-board computer each 4 seconds.

3.3. Data acquisition

The evolution of the water temperature with depth during the descent of the probe was recorded at each heat flow site. It allowed to measure the thermal gradient in the water column, as well as the temperature jump due to frictional heating upon penetration. The heating rate of each thermal conductivity sensor was recorded during 6 minutes starting 40 s after penetration, while the temperature–time evolution at the "G-line" was recorded during 10 minutes (for an example see Fig. 5). The heating effects upon penetration were removed by calculating the asymptotic temperature value with an exponential fitting. Heat flow density was therefore calculated as the weighted mean between the different depth intervals.

At most of the heat flow sites, the measured temperature at the lowermost sensor was anomalously low during the penetration of the probe into the sediments. After a careful analysis of the data, we concluded that this phenomenon was probably due to a thermal distortion produced during the penetration of the probe (the sensor is placed at 15 cm from the end of the supporting rod). For this reason, the temperature measurements at 2.0 m depth were rejected. This anomalous behaviour influences

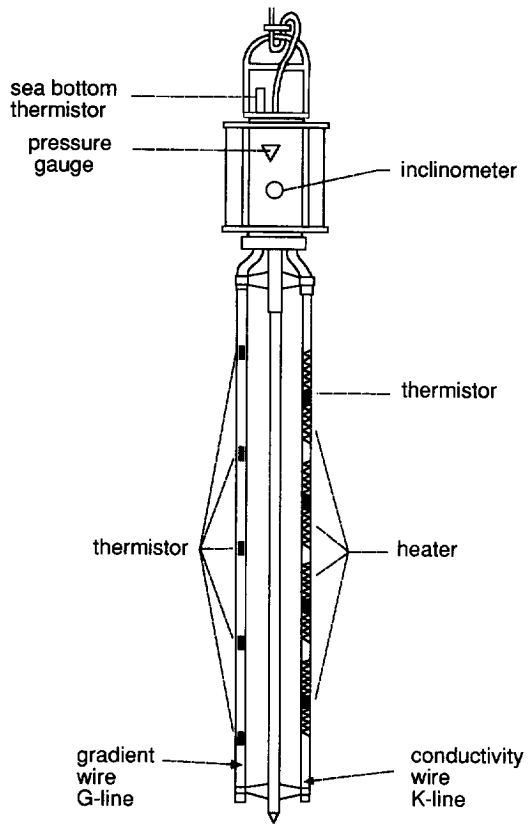

Fig. 4. Schematic diagram of the GEOS-3M probe and its main components.

the absolute temperature values at the upper sensors, but not the temperature differences between them.

4. Results

4.1. Thermal conductivity

Thermal conductivity of sediments was measured "in situ" at 86 sites. Each site consists of four measurements carried out 0.5 m depth intervals from the sea bottom. The obtained results are summarized in Table 1. Thermal conductivity values range from 0.78 to 1.56 $W m^{-1} K^{-1}$, with an average value for the whole basin of 1.27 ± 0.06 $W m^{-1}$.

The uppermost sedimentary cover in the Alboran Basin is made up by silty clays and muds. Preliminary results, based on water content, granulometry (sand, silt, and clay content) and carbonate content analyses carried out on the gravity cores, show major spatial (lateral and vertical) variations of these parameters. On average, the sediments are composed by 20–35% silt, 60–80% clay and 3–7% sand, except in the Yusuff Basin where the sand content reaches 60%. The carbonate content varies between 18 and 34%. The water content ranges from 28 to 70%, the highest values corresponding to the upper-

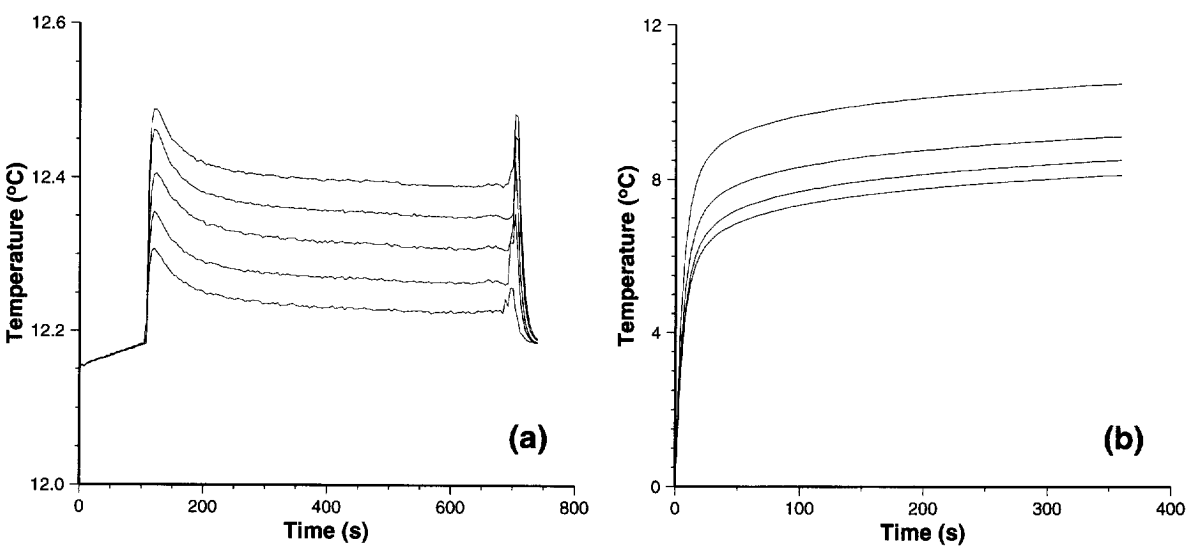

Fig. 5. Temperature–time records at site #96. (a) Thermal gradient line. Relative maxima at 120 and 700 s are produced by frictional effects during penetration and extraction of the probe. (b) Thermal conductivity line.

Table 1
Thermal conductivity of sediments

Site	Water depth	Thermal conductivity (k) W m^{-1} K^{-1}						
(#)	(m)	0–0.5 m	0.5–1 m	1–1.5 m	1.5–2 m	Mean ± 5% (err)	SD (k)	SD ($1/k$)
Profile WAB-1 (N–S)								
5	597	1.40	1.26	1.42	1.53	1.40 ± 0.07	0.11	0.06
6	700	1.43	1.24	1.34	1.46	1.36 ± 0.07	0.10	0.05
9	891	1.26	1.21	1.32	1.22	1.25 ± 0.06	0.05	0.03
13	1090	1.30	1.24	1.30	1.28	1.28 ± 0.06	0.03	0.02
14	1200	1.33	1.23	1.34	1.25	1.29 ± 0.06	0.06	0.03
15	1258	1.22	1.24	1.29	1.24	1.25 ± 0.06	0.03	0.02
63	1023	1.24	1.26	1.34	1.29	1.28 ± 0.06	0.04	0.03
64	1125	1.27	1.29	1.38	1.24	1.29 ± 0.06	0.06	0.03
65	1171	1.20	1.23	1.25	1.21	1.22 ± 0.06	0.02	0.01
17	1286	1.33	1.26	1.33	1.24	1.29 ± 0.06	0.05	0.03
18	1283	1.25	1.27	1.29	1.22	1.26 ± 0.06	0.03	0.02
19	1362	1.32	1.24	1.26	1.20	1.25 ± 0.06	0.05	0.03
20	1394	1.39	1.29	1.30	1.28	1.31 ± 0.07	0.05	0.03
21	1439	1.25	1.24	1.33	1.25	1.27 ± 0.06	0.04	0.03
22	1470	1.29	1.22	1.22	1.16	1.22 ± 0.06	0.05	0.04
23	1480	1.33	1.22	1.28	1.27	1.27 ± 0.06	0.05	0.03
24	1473	1.56	1.18	1.26	1.19	1.28 ± 0.06	0.18	0.10
25	1445	1.22	1.18	1.26	1.20	1.21 ± 0.06	0.03	0.02
Profile WAB-2 (W–E)								
53	934	1.20	1.25	1.22	1.25	1.23 ± 0.06	0.02	0.02
54	978	1.17	1.26	1.32	1.26	1.25 ± 0.06	0.06	0.04
55	1055	1.26	1.26	1.40	1.26	1.29 ± 0.06	0.07	0.04
56	1085	1.31	1.31	1.32	1.23	1.29 ± 0.06	0.04	0.03
57	1142	0.78	1.11	1.42	1.22	1.08 ± 0.05	0.27	0.25
58	1178	1.31	1.25	1.23	1.26	1.26 ± 0.06	0.03	0.02
59	1211	1.29	1.24	1.31	1.21	1.26 ± 0.06	0.05	0.03
61	1280	1.34	1.30	1.42	1.35	1.35 ± 0.07	0.05	0.03
67	1292	1.26	1.22	1.25	1.22	1.24 ± 0.06	0.02	0.01
68	1266	1.31	1.25	1.28	1.28	1.28 ± 0.06	0.02	0.01
69	1308	1.22	1.26	1.31	1.29	1.27 ± 0.06	0.04	0.02
70	1310	1.29	1.31	1.32	1.30	1.30 ± 0.07	0.01	0.01
71	1306	1.21	1.23	1.25	1.23	1.23 ± 0.06	0.02	0.01
72	1294	1.18	1.12	1.20	1.18	1.17 ± 0.06	0.03	0.03
73	1282	1.22	1.17	1.28	1.22	1.22 ± 0.06	0.05	0.03
74	1244	1.15	1.19	1.18	1.11	1.16 ± 0.06	0.04	0.03
3	1197	1.37	1.26	1.29	1.27	1.30 ± 0.06	0.05	0.03
Profile WAB-3 (SE–NW)								
43	949	1.15	1.27	1.29	1.22	1.23 ± 0.06	0.06	0.04
44	932	1.24	1.17	1.23	1.23	1.22 ± 0.06	0.03	0.02
45	885	1.29	1.21	1.30	1.28	1.27 ± 0.06	0.04	0.03
46	807	1.28	1.23	1.31	1.23	1.26 ± 0.06	0.04	0.02
47	715	1.22	1.30	1.30	1.27	1.27 ± 0.06	0.04	0.02
48	672	1.47	1.28	1.26	1.21	1.30 ± 0.06	0.11	0.06
Profile WAB-4 (SW–NE)								
32	461	1.38	1.36	1.36	1.38	1.37 ± 0.07	0.01	0.01
33	541	1.34	1.33	1.39	1.41	1.37 ± 0.07	0.04	0.02
34	715	1.20	1.42	1.29	1.35	1.31 ± 0.07	0.09	0.05
35	1062	1.32	1.27	1.30	1.26	1.29 ± 0.06	0.03	0.02
37	1074	1.23	1.25	1.29	1.24	1.25 ± 0.06	0.03	0.02
38	1050	1.29	1.31	1.35	1.27	1.30 ± 0.07	0.03	0.02
40	1055	1.30	1.27	1.36	1.30	1.31 ± 0.07	0.04	0.02

Table 1 (continued)

Site	Water depth	Thermal conductivity (k) W m^{-1} K^{-1}						
(#)	(m)	0–0.5 m	0.5–1 m	1–1.5 m	1.5–2 m	Mean ± 5% (err)	SD (k)	SD ($1/k$)
Profile WAB-4 (SW–NE)								
41	1112	1.28	1.25	1.31	1.30	1.28 ± 0.06	0.03	0.02
Profile EAB-1 (W–E)								
77	1787	1.29	1.35	1.31	1.24	1.30 ± 0.06	0.05	0.03
78	1779	1.34	1.44	1.33	1.28	1.35 ± 0.07	0.07	0.04
79	1750	1.32	1.22	1.23	1.22	1.25 ± 0.06	0.05	0.03
80	1751	1.33	1.40	1.35	1.27	1.34 ± 0.07	0.05	0.03
Profile EAB-2 (W–E)								
82	1900	1.29	1.18	1.16	1.15	1.19 ± 0.06	0.06	0.04
83	1902	1.36	1.28	1.20	1.18	1.25 ± 0.06	0.08	0.05
84	1892	1.33	1.19	1.17	1.17	1.21 ± 0.06	0.08	0.05
85	1725	1.38	1.30	1.27	1.28	1.31 ± 0.07	0.05	0.03
86	1820	1.37	1.29	1.28	1.26	1.30 ± 0.06	0.05	0.03
88	1883	1.35	1.21	1.21	1.23	1.25 ± 0.06	0.07	0.04
89	1892	1.33	1.17	1.17	1.22	1.22 ± 0.06	0.08	0.05
91	1993	1.31	1.21	1.20	1.22	1.23 ± 0.06	0.05	0.03
92	2310	1.39	1.19	1.19	1.26	1.25 ± 0.06	0.09	0.06
93	2383	1.27	1.14	1.13	1.17	1.18 ± 0.06	0.06	0.04
94	2431	1.27	1.14	1.11	1.15	1.16 ± 0.06	0.07	0.05
95	2480	1.34	1.19	1.25	1.23	1.25 ± 0.06	0.06	0.04
96	2515	1.35	1.45	1.36	1.38	1.38 ± 0.07	0.05	0.02
Profile YB-1								
100	2292	1.24	1.24	1.28	1.27	1.26 ± 0.06	0.02	0.01
101	2287	1.28	1.30	1.40	1.38	1.34 ± 0.07	0.06	0.03
Profile SAB-1 (NE–SW)								
109	1053	1.14	1.13	1.21	1.21	1.17 ± 0.06	0.04	0.03
110	1106	1.23	1.31	1.39	1.38	1.32 ± 0.07	0.07	0.04
111	1118	1.16	1.19	1.23	1.26	1.21 ± 0.06	0.04	0.03
112	1098	1.12	1.17	1.21	1.21	1.18 ± 0.06	0.04	0.03
113	1069	1.16	1.16	1.28	1.27	1.21 ± 0.06	0.07	0.04
114	1092	1.17	1.18	1.26	1.27	1.22 ± 0.06	0.05	0.04
116	1133	1.15	1.25	1.20	1.24	1.21 ± 0.06	0.05	0.03
117	1094	1.13	1.18	1.26	1.24	1.20 ± 0.06	0.06	0.04
Profile SAB-2 (N–S)								
102	1082	1.23	1.28	1.32	1.29	1.28 ± 0.06	0.04	0.02
103	1116	1.35	1.29	1.37	1.31	1.33 ± 0.07	0.04	0.02
104	1118	1.29	1.24	1.31	1.28	1.28 ± 0.06	0.03	0.02
106	1123	1.10	1.11	1.25	1.14	1.15 ± 0.06	0.07	0.05
107	1075	1.18	1.22	1.26	1.26	1.23 ± 0.06	0.04	0.03
108	851	1.10	1.13	1.28	1.25	1.19 ± 0.06	0.09	0.06
Profile DB-1 (N–S)								
120	894	1.28	1.36	1.34	1.37	1.34 ± 0.07	0.04	0.02
123	959	1.32	1.37	1.29	1.26	1.31 ± 0.07	0.05	0.03
124	874	1.35	1.36	1.32	1.31	1.33 ± 0.07	0.02	0.01
125	813	1.32	1.42	1.40	1.39	1.38 ± 0.07	0.04	0.02
126	774	1.47	1.44	1.54	1.40	1.46 ± 0.07	0.06	0.03
Average:		1.26	1.29	1.25	1.27	1.27		
Dispersion:		0.005	0.005	0.006	0.010	0.004		
SD:		0.070	0.072	0.076	0.101	0.062		

Table 2
Sea floor heat flow in the Alboran Sea

Site	Lat.	Long.	Water depth	Bottom water T	Up. sens. depth	Up. sens. T	Thermal grad. interv. (mK/m)					k (W/mK)		q (mW/m^2)		Tilt
(#)	(°N)	(°W)	(m)	(°C)	(m)	(°C)	0–0.5	0.5–1	1–1.5	Mean	Err	Mean	Err	Mean	Err	(°)
Profile WAB-1 (N–S)																
4	36-25.4	4-26.8	466	12.176	> 0	12.111	31	38	22	30	2.0	1.36 [a]		> 42		8
5	36-23.0	4-25.3	597	12.062	> 0	12.014	37	36	29	34	2.0	1.36	0.07	> 46	5	8
6	36-20.8	4-23.7	700	12.038	> 0	11.989	29	37	24	30	2.0	1.33	0.07	> 40	5	1
7	36-18.4	4-20.6	803	11.991	> 0	11.979	52	44	45	47	2.0	1.26 [a]		59		11
9	36-16.2	4-19.5	891	11.975	0.03	11.976	57	57	56	57	2.0	1.26	0.06	72	6	72
10	36-15.0	4-18.9	952	11.991	> 0	11.970	74	59	60	64	2.0	1.27 [a]		81		18
13	36-12.5	4-19.3	1090	11.995	0.54	12.039	85	72	84	80	2.0	1.28	0.06	103	8	5
14	36-09.2	4-18.5	1200	11.986	0.68	12.042	87	75	78	80	2.0	1.30	0.06	104	8	15
15	36-06.5	4-19.5	1258	12.000	0.59	12.039	69	59	60	63	2.0	1.25	0.06	78	6	9
62	36-11.6	4-21.0	1109	11.976	0.75	12.030	74	69	70	71	2.0	1.29 [a]		92		6
63	36-14.3	4-19.6	1023	12.021	0.15	12.031	69	63	66	66	2.0	1.28	0.06	84	7	2
64	36-10.9	4-19.0	1125	11.981	0.67	12.043	93	88	99	93	2.0	1.31	0.07	123	9	3
65	36-10.8	4-17.0	1171	11.983	0.68	12.044	93	80	87	87	2.0	1.23	0.06	106	8	2
17	36-00.5	4-20.4	1286	12.003	0.63	12.051	79	69	74	74	2.0	1.31	0.07	97	7	6
18	35-57.6	4-20.9	1283	12.003	0.52	12.035	62	61	57	60	2.0	1.27	0.06	76	6	4
19	35-54.7	4-21.0	1362	12.001	0.59	12.037	62	64	60	62	2.0	1.27	0.06	79	6	2
20	35-52.2	4-21.0	1394	12.012	0.57	12.045	57	58	61	59	2.0	1.33	0.07	78	7	5
21	35-49.5	4-21.5	1439	12.014	0.76	12.058	57	67	44	56	2.0	1.27	0.06	71	6	6
22	35-47.2	4-21.2	1470	12.020	0.67	12.059	58	55	66	60	2.0	1.24	0.06	74	6	7
23	35-44.1	4-21.1	1480	12.021	0.66	12.059	58	62	47	56	2.0	1.28	0.06	71	6	3
24	35-41.7	4-21.0	1473	12.029	0.62	12.061	52	49	57	53	2.0	1.31	0.07	70	6	6
25	35-39.0	4-21.3	1445	12.020	0.58	12.056	66	57	47	57	2.0	1.22	0.06	69	6	4
Profile WAB-2 (W–E)																
53	36-03.4	4-48.6	934	11.965	0.65	11.984	30	28	37	32	2.0	1.22	0.06	> 39	4	5
54	36-04.0	4-44.9	978	11.970	0.73	12.002	49	31	45	42	2.0	1.25	0.06	52	5	5
55	36-03.7	4-41.1	1055	11.968	0.82	11.999	43	25	46	38	2.0	1.30	0.07	50	5	4
56	36-03.4	4-38.1	1085	11.975	0.61	12.000	43	36	44	41	2.0	1.31	0.07	54	5	4
57	36-03.4	4-34.4	1142	11.979	0.72	12.010	41	49	48	46	2.0	1.28 [a]		59		9
58	36-03.7	4-31.2	1178	11.989	0.61	12.021	57	48	44	50	2.0	1.26	0.06	63	6	5
59	36-03.7	4-27.7	1211	11.991	0.61	12.030	67	59	60	62	2.0	1.28	0.06	79	7	7
60	36-03.3	4-23.7	1248	11.994	0.04	11.997	69	70	79	73	2.0	1.30 [a]		95		22
61	36-02.5	4-20.6	1280	12.000	0.60	12.046	85	65	67	72	2.0	1.35	0.07	98	8	6
67	36-03.6	4-17.7	1292	11.997	0.71	12.043	69	58	63	63	2.0	1.24	0.06	79	6	7
68	36-03.7	4-21.1	1266	11.998	0.62	12.045	81	68	67	72	2.0	1.28	0.06	92	7	4
69	36-03.6	4-14.2	1308	12.003	0.72	12.045	63	48	62	58	2.0	1.26	0.06	73	6	7
70	36-03.8	4-11.0	1310	12.004	0.62	12.047	71	63	71	68	2.0	1.31	0.07	89	7	3
71	36-04.0	4-08.0	1306	12.002	0.68	12.052	76	66	77	73	2.0	1.23	0.06	90	7	5
72	36-04.0	4-04.3	1294	11.999	0.63	12.049	81	77	78	79	2.0	1.17	0.06	92	7	2

73	36-04.3	4-01.4	1282	11.998	0.65	12.048	76	72	89	79	2.0	1.22	0.06	97	7	3
74	36-04.4	3-58.5	1244	11.990	0.64	12.047	97	78	82	86	2.0	1.17	0.06	100	7	7
3	36-03.7	3-55.2	1197	11.983	0.07	11.990	90	93	84	89	2.0	1.31	0.07	116	8	6
Profile WAB-3 (SE–NW)																
43	36-04.3	4-47.4	949	11.966	> 0	11.997	34	22	35	30	2.0	1.23	0.06	> 37	4	6
44	36-07.2	4-48.2	932	11.990	0.45	12.003	27	30	38	32	2.0	1.21	0.06	> 38	4	2
45	36-09.8	4-49.9	885	12.001	0.36	12.011	27	25	38	30	2.0	1.27	0.06	> 38	4	4
46	36-12.2	4-51.2	807	12.031	> 0	12.010	30	18	30	26	2.0	1.27	0.06	> 33	4	3
47	36-14.5	4-52.6	715	12.052	> 0	12.013	37	20	24	27	2.0	1.27	0.06	> 34	4	11
48	36-16.1	4-53.2	672	12.076	> 0	12.027	25	25	21	24	2.0	1.33	0.06	> 31	4	8
Profile WAB-4 (SW–NE)																
31	35-46.3	5-00.4	414	11.876	> 0	11.950	48	46	45	46	2.0	1.37 [a]		< 63		5
32	35-48.2	4-57.4	461	11.877	> 0	11.932	36	35	40	37	2.0	1.37	0.07	< 51	5	7
33	35-49.4	4-54.8	541	11.891	> 0	11.931	41	31	27	33	2.0	1.35	0.07	< 45	5	4
34	35-51.0	4-51.6	715	11.915	0.91	11.947	40	25	35	33	2.0	1.30	0.06	< 43	5	15
35	35-52.8	4-48.7	1062	11.996	> 0	11.992	40	41	44	42	2.0	1.30	0.06	54	5	4
37	35-54.5	4-46.1	1074	11.973	0.62	11.997	40	37	38	38	2.0	1.26	0.06	48	5	5
38	35-55.9	4-43.1	1050	11.966	0.73	11.996	42	39	36	39	2.0	1.32	0.07	51	5	6
40	35-57.2	4-40.5	1055	11.965	0.59	11.989	45	34	42	40	2.0	1.31	0.07	53	5	4
41	35-58.7	4-37.9	1112	11.975	0.58	12.001	47	39	38	41	2.0	1.28	0.06	53	5	7
Profile EAB-1 (W–E)																
76	36-10.7	2-42.7	1809	12.066	0.51	12.112	93	81	97	90	2.0	1.32 [a]		119		3
77	36-11.5	2-39.3	1787	12.069	0.49	12.114	95	90	96	94	2.0	1.32	0.07	123	9	5
78	36-12.3	2-36.2	1779	12.067	0.44	12.111	104	94	93	97	2.0	1.37	0.07	133	9	4
79	36-13.5	2-30.0	1750	12.062	0.50	12.105	92	77	93	87	2.0	1.26	0.06	110	8	3
80	36-14.8	2-23.4	1751	12.064	0.48	12.107	89	86	99	91	2.0	1.36	0.07	124	9	4
Profile EAB-2 (W–E)																
82	36-13.4	2-02.5	1900	12.088	0.56	12.135	81	85	96	87	2.0	1.21	0.06	105	8	4
83	36-12.1	2-01.4	1902	12.087	0.64	12.135	74	69	84	76	2.0	1.28	0.06	97	7	5
84	36-14.9	2-04.1	1892	12.084	0.61	12.137	81	96	97	91	2.0	1.23	0.06	112	8	4
85	36-18.1	2-02.4	1725	12.065	0.51	12.110	88	85	90	88	2.0	1.32	0.07	115	8	3
86	36-18.0	1-59.1	1820	12.075	0.60	12.128	85	93	98	92	2.0	1.31	0.07	121	9	4
87	36-17.8	1-55.8	1846	12.078	0.57	12.136	108	90	93	97	2.0	1.28 [a]		124		6
88	36-17.9	1-52.3	1883	12.089	0.54	12.145	106	100	99	102	2.0	1.25	0.06	128	9	4
89	36-18.2	1-45.6	1892	12.094	0.58	12.157	108	107	122	112	2.0	1.22	0.06	137	9	6
91	36-17.8	1-39.2	1993	12.100	0.66	12.163	87	111	93	97	2.0	1.24	0.06	120	8	3
92	36-18.0	1-32.8	2310	12.154	0.58	12.208	89	99	100	96	2.0	1.25	0.06	120	8	1
93	36-17.8	1-29.3	2383	12.165	0.59	12.226	113	81	113	102	2.0	1.18	0.06	121	8	2
94	36-18.0	1-25.9	2431	12.172	0.51	12.220	93	96	95	95	2.0	1.17	0.06	111	8	1

Table 2 (continued)

Site	Lat.	Long.	Water depth	Bottom water T	Up. sens. depth	Up. sens. T	Thermal grad. interv. (mK/m)					k (W/mK)		q (mW/m^2)		Tilt
(#)	(°N)	(°W)	(m)	(°C)	(m)	(°C)	0–0.5	0.5–1	1–1.5	Mean	Err	Mean	Err	Mean	Err	(°)
Profile EAB-2 (W–E)																
95	36-18.1	1-19.7	2480	12.180	0.61	12.229	79	81	88	83	2.0	1.26	0.06	104	8	1
96	36-17.5	1-11.4	2515	12.188	0.45	12.224	77	89	82	83	2.0	1.39	0.07	115	8	1
97	36-17.8	1-06.0	2530	12.192	0.005	12.192	98	93	87	93	2.0	1.39 [a]		129		
Profile YB-1																
100	35-52.4	1-56.0	2292	12.155	1.14	12.258	95	76	103	91	2.0	1.25	0.06	115	8	3
101	35-53.0	1-59.9	2287	12.154	0.76	12.221	90	83	90	88	2.0	1.32	0.07	116	8	3
Profile SAB-1 (NE–SW)																
109	35-43.0	3-12.2	1053	11.956	0.73	12.030	100	104	102	102	2.0	1.16	0.06	118	8	5
110	35-42.0	3-16.6	1106	11.967	0.63	12.036	111	111	100	107	2.0	1.31	0.07	140	10	2
111	35-40.6	3-19.2	1118	11.968	0.66	12.037	111	91	98	100	2.0	1.19	0.06	119	8	4
112	35-38.5	3-23.0	1098	11.963	0.76	12.035	91	100	102	98	2.0	1.17	0.06	114	8	2
113	35-37.2	3-25.5	1069	11.960	0.71	12.028	102	83	93	93	2.0	1.20	0.06	111	8	2
114	35-33.0	3-19.0	1092	11.967	0.71	12.059	131	129	121	127	2.0	1.20	0.06	153	10	4
116	35-35.2	3-19.0	1133	11.972	0.76	12.050	109	91	94	98	2.0	1.20	0.06	117	8	5
117	35-41.0	3-21.2	1094	11.965	0.70	12.038	103	107	106	105	2.0	1.19	0.06	125	9	2
Profile SAB-2 (N–S)																
102	36-00.9	2-37.9	1082	11.951	0.55	12.000	89	91	79	86	2.0	1.28	0.06	110	8	4
103	35-58.9	2-40.1	1116	11.962	0.64	12.024	98	100	86	95	2.0	1.34	0.07	126	9	4
104	35-57.5	2-42.8	1118	11.960	0.64	12.023	100	97	93	97	2.0	1.28	0.06	124	9	4
106	35-56.0	2-45.5	1123	11.963	0.61	12.025	108	91	84	94	2.0	1.15	0.06	108	8	4
107	35-53.2	2-45.8	1075	11.968	0.68	12.033	95	95	88	93	2.0	1.22	0.06	113	8	5
108	35-50.3	2-45.5	851	11.944	0.55	12.001	103	106	100	103	2.0	1.16	0.06	120	8	6
Profile DB-1 (N–S)																
119	36-31.5	3-14.7	846	12.038	0.68	12.075	47	62	71	60	2.0	1.33 [a]		> 80		13
120	36-27.9	3-15.8	894	11.986	0.60	12.039	91	79	86	85	2.0	1.33	0.07	> 113	8	3
122	36-23.4	3-18.3	949	12.002	0.49	12.047	96	82	91	90	2.0	1.33 [a]		> 120		15
123	36-24.3	3-17.0	959	11.998	0.54	12.053	106	89	100	98	2.0	1.33	0.07	> 130	9	14
124	36-19.6	3-18.1	874	11.986	0.60	12.046	106	90	95	97	2.0	1.34	0.07	> 130	9	2
125	36-11.7	3-20.9	813	11.974	0.65	12.097	193	185	174	184	2.0	1.38	0.07	> 254	15	3
126	36-13.5	3-20.6	774	11.966	0.35	12.018	152	136	133	140	2.0	1.48	0.07	> 208	13	12

k indicates thermal conductivity and q indicates sea floor heat flow.

[a] Thermal conductivity has been taken from nearly sites.

most levels. The layered structure observed in the cores with alternating high and low porosities is responsible for the vertical variations of thermal conductivity (Table 1). Spatially, the highest average water content corresponds to the South Alboran Basin (52%) where the average thermal conductivity is 1.23 ± 0.05 W m^{-1} K^{-1}. In contrast, the lowest average water content corresponds to the Western Alboran Basin (45%) where the average thermal conductivity is 1.27 ± 0.05 W m^{-1} K^{-1}. In the Djibouti Bank (Fig. 1), the average thermal conductivity is 1.36 ± 0.06 W m^{-1} K^{-1}. Only one sedimentary core was recovered in this area, which does not permit to draw firm conclusions about the high thermal conductivity. Therefore, although there is no clear evidence for a systematic increase of conductivity with depth, its spatial variation appears to be closely related to texture and water content.

4.2. Measured heat flow

Heat flow was successfully measured at 98 sites, 86 of them having "in situ" thermal conductivity measurements. At the other twelve sites, trembling of the probe during thermal conductivity measurements distorted the results and therefore, this parameter was estimated from neighbouring sites. Table 2 summarizes the obtained results. The measured heat flow varies from 31 (site #48) to 254 (site #125) mW m^{-2} and its spatial distribution shows that the Western Alboran Basin differs noticeably from the Eastern and Southern Alboran basins (Table 3). For clarity, we have split up the study area in two zones: the Western Alboran Basin (WAB) and the Eastern Alboran Basin (EAB), the latter includes also the South Alboran Basin (SAB) and the Djibouti Bank (DB).

4.2.1. The Western Alboran Basin (WAB)

A total of 55 heat flow measurements were performed in the WAB resulting in an average value of 69 ± 6 mW m^{-2} (s.d. ± 24 mW m^{-2}). The spatial distribution of the measured heat flow values is shown in Fig. 6. The most striking feature is the clear heat flow increase both eastwards and towards the centre of the basin. The lower values correspond to the northwestern and northern parts of the WAB, where heat flow ranges from 31 to 52 mW m^{-2}. The southwestern WAB is characterized by a heat flow that ranges in value from 43 to 63 mW m^{-2}, whereas the southern part shows a northward increase from 69 to 98 mW m^{-2}. Along the E–W-trending central axis of the basin, the heat flow increases eastwards from 52 to 116 mW m^{-2}.

The measured heat flow values along two E–W- and N–S-oriented seismic and gravity profiles are shown in Fig. 8. The free-air anomaly data have been reduced to the Postdam datum and a density reduction of 2670 kg m^{-3} has been applied to obtain the "simple Bouguer" anomaly (without topographic correction). Heat flow shows a strong positive correlation with Bouguer anomaly. However, the presence of very thick sedimentary sequences (up to 5 s twtt) in both profiles, which masks the deep gravity signature, makes it difficult to attribute the heat flow variations to crustal/lithospheric thinning. Furthermore, the high sedimentation rate in these small basins could produce a significant cooling effect which could be the cause, at least partially, of the observed low heat flow values. Heat flow corrections due to sediments effects will be discussed in the next section.

Superimposed over this regional heat flow pattern, there are two local thermal anomalies. One of them is located at the intersection of the N–S- and E–W-oriented heat flow trajects, where four closely located sites (#17, 60, 61 and 68, Table 2) show heat flow values between 92 and 98 mW m^{-2} (about 10–15 mW m^{-2} above the average regional value). Several kilometers to the north and coinciding with the location of the DSDP Site 121, the measured heat flow at sites #13, 14, 64 and 65 displays values higher than 100 mW m^{-2}, reaching a maximum of 123 mW m^{-2} (Table 2; Fig. 7). Although both anomalies are spatially confined to a basement high, it is not evident — as will be discussed in the next section — that these high heat flow values are due only to thermal refraction effects.

4.2.2. The Eastern Alboran basin (EAB, SAB and DB)

The Eastern Alboran Basin, which opens to the South Balearic Basin with an oceanic crust type (Galdeano and Rossignol, 1977; Morelli, 1985; Rehault et al., 1985), as well as the trough-like South Alboran Basin and the Djibouti Bank, show a heat

Table 3
Heat flow statistics in the Alboran Basin

Zones	Site number	Heat flow density (mW/m^2)			
		Min	Max	St. dev.	Mean
WAB	55	31	122	24	69±6
SAB	14	109	153	12	121±6
Yusuff Bas.	2	114	117		
EAB	27	80	254	33	126±12
	25	80	137	12	118±4
SAB+Yb+EAB	43	80	254	27	124±8
	41	80	153	12	119±4

flow pattern (Fig. 9) very different from the one observed in the Western Alboran Basin. The heat flow density in both the EAB and SAB is fairly constant, with a mean value of 121–126 $mW\,m^{-2}$ (Table 3). This value is almost twice as high as that in the WAB. Thus, the eastward increase in heat flow density observed in the WAB continues until the Alboran Ridge and remains roughly constant for the overall EAB.

The heat flow values obtained along an E–W-oriented seismic and gravity profile are shown in Fig.

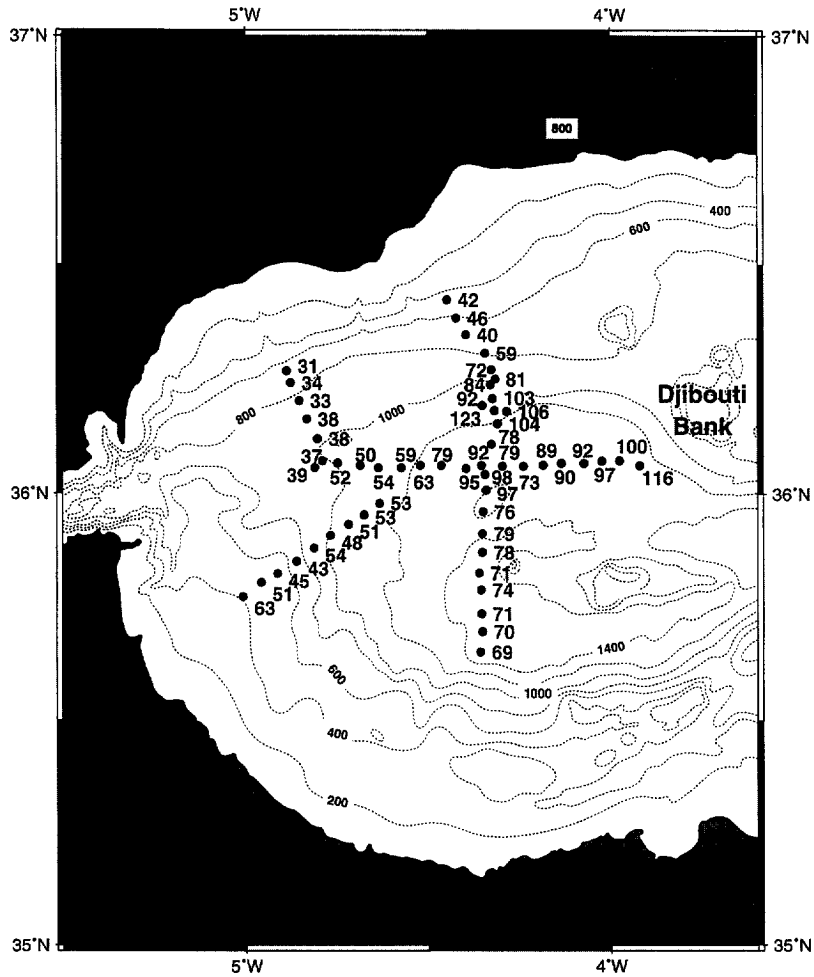

Fig. 6. Measured heat flow in the West Alboran Basin ($mW\,m^{-2}$). Contour interval for bathymetry is 200 m.

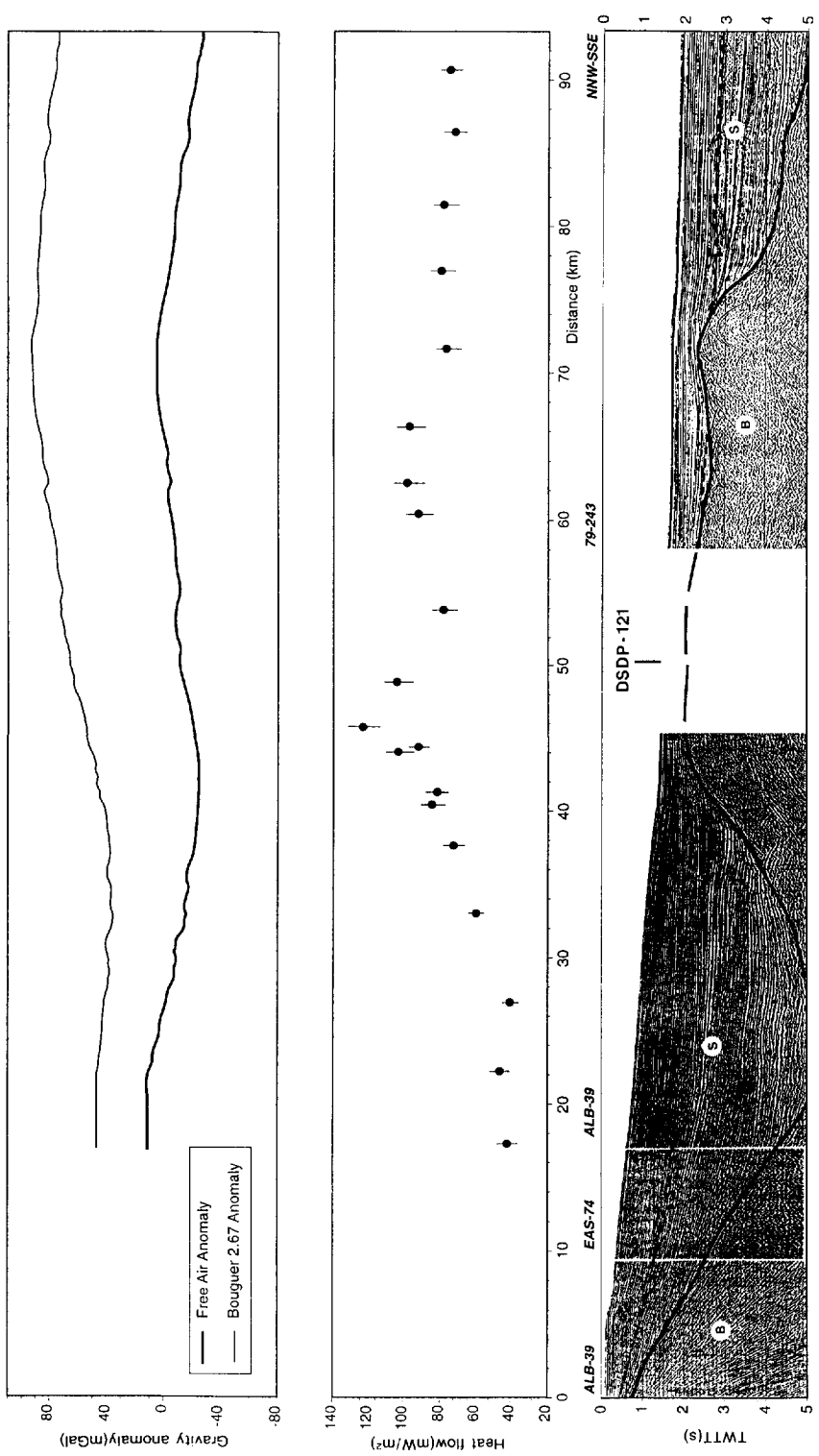

Fig. 7. Composed heat flow, gravity and seismic profile corresponding to the WAB-1 heat flow trajFig. 7 and Fig. 3). S = Neogene–Quaternary sedimentary cover; B = acoustic basement. Dotted line indicates the Miocene–Pliocene limit.

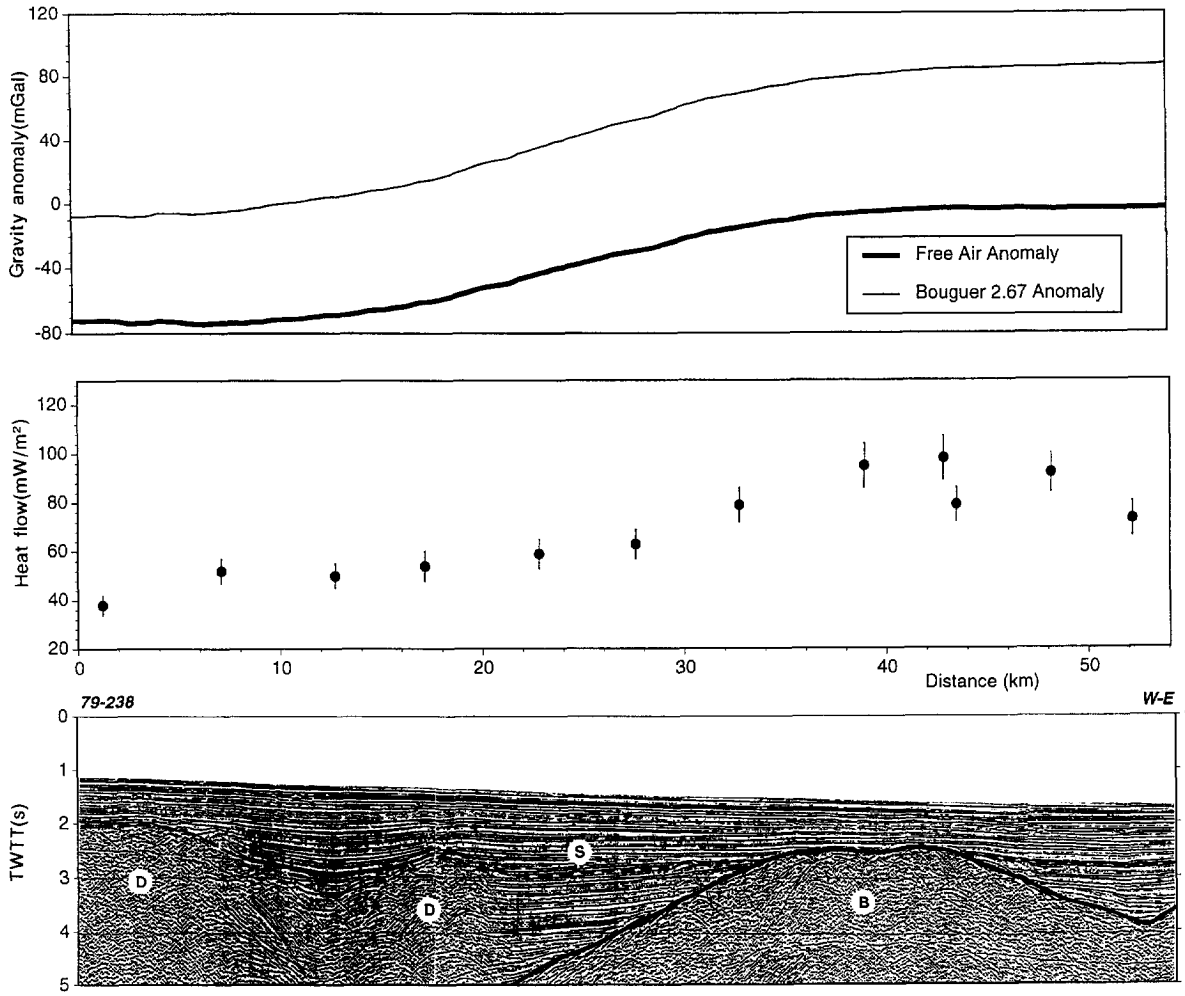

Fig. 8. Composed heat flow, gravity and seismic profile corresponding to the WAB-2 heat flow traject (Fig. 3). S = Neogene–Quaternary sedimentary cover; B = acoustic basement; D = mud diapirs. Dotted line indicates the Miocene–Pliocene limit.

10. In this case, the Bouguer gravity anomaly increases smoothly eastwards where the basin deepens. However, this increase, which exceeds 55 mGal, does not correlate with an increase in heat flow. This fact raises a major question in the interpretation of the Alboran Sea evolution as we will discuss later.

Superimposed over this rather constant heat flow trend, two local thermal anomalies have been identified in the Djibouti Bank and in the SAB. The strongest positive heat flow anomaly in the Alboran Sea occurs in the eastern Djibouti Bank (Fig. 9). The heat flow density reaches a maximum value of 254 mW/m^{-2} (site #125) decreasing northward to 80 mW/m^2 (site #119). The influence of the volcanic high close to this anomaly will be discussed in the following sections. The SAB thermal anomaly (up to 153 mW/m^2) is restricted to the southernmost SAB and is probably associated with recent SW–NE-trending strike-slip faults (see Fig. 2).

5. Heat flow corrections

Surface heat flow density measurements are affected by different shallow processes that perturb the background thermal field associated with the litho-

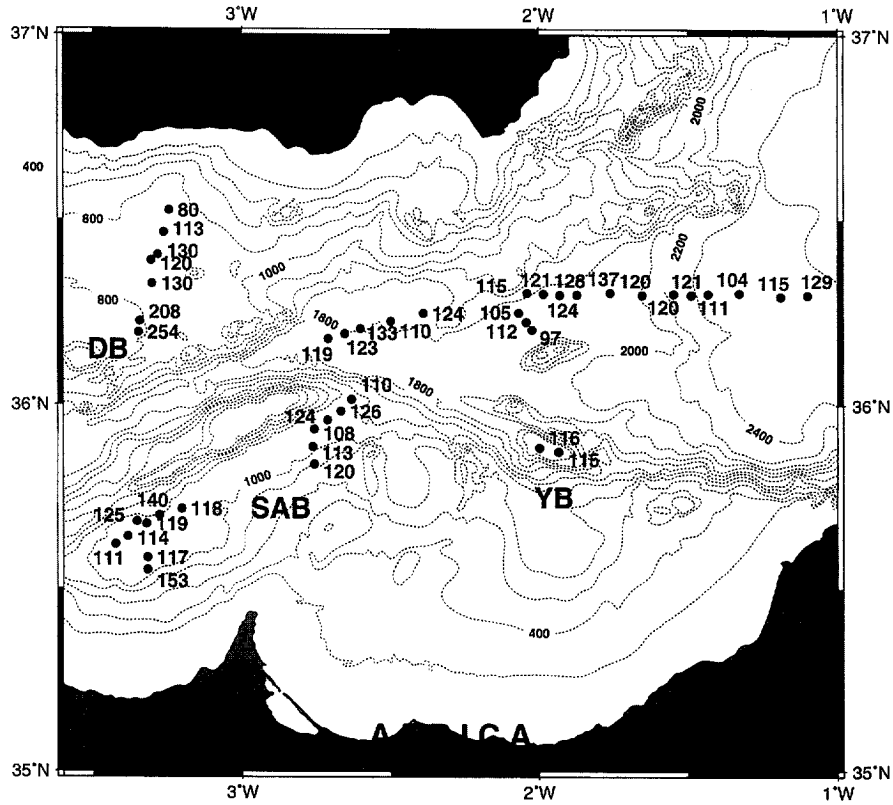

Fig. 9. Measured heat flow in the East Alboran Basin (mW m^{-2}). Contour interval for bathymetry is 200 m.

spheric structure. Therefore, measured heat flow values must be corrected for these processes in order to infer the regional lithospheric thermal structure. These processes can be grouped as follows: those that produce steady-state thermal perturbations and those that produce transient effects.

5.1. Steady-state corrections

Steady-state corrections include thermal refraction associated with both sea bottom topography and lateral variation of thermal conductivity. In order to quantify these effects, we have selected the N–S-oriented heat flow profile in the WAB where major variations in basement topography and sedimentary infill occur. To this profile we have applied a numerical finite element model that solves the 2-D thermal conduction equation in the absence of heat production sources.

A schematic cross section deduced from a N–S-oriented seismic profile (see Fig. 7), where we have distinguished two sedimentary layers and the acoustic basement, is shown in Fig. 11. To maximize the thermal refraction effects we have considered a maximum thermal conductivity contrast. Therefore, the uppermost sedimentary layer, which is roughly 1 km thick, corresponds to Pliocene–Recent sediments and is assumed to have a low thermal conductivity (1.3 W m^{-1} K^{-1}) according to sea bottom measurements (Table 1) and low sediment compaction (Jurado and Comas, 1992). The lower sedimentary layer, Miocene

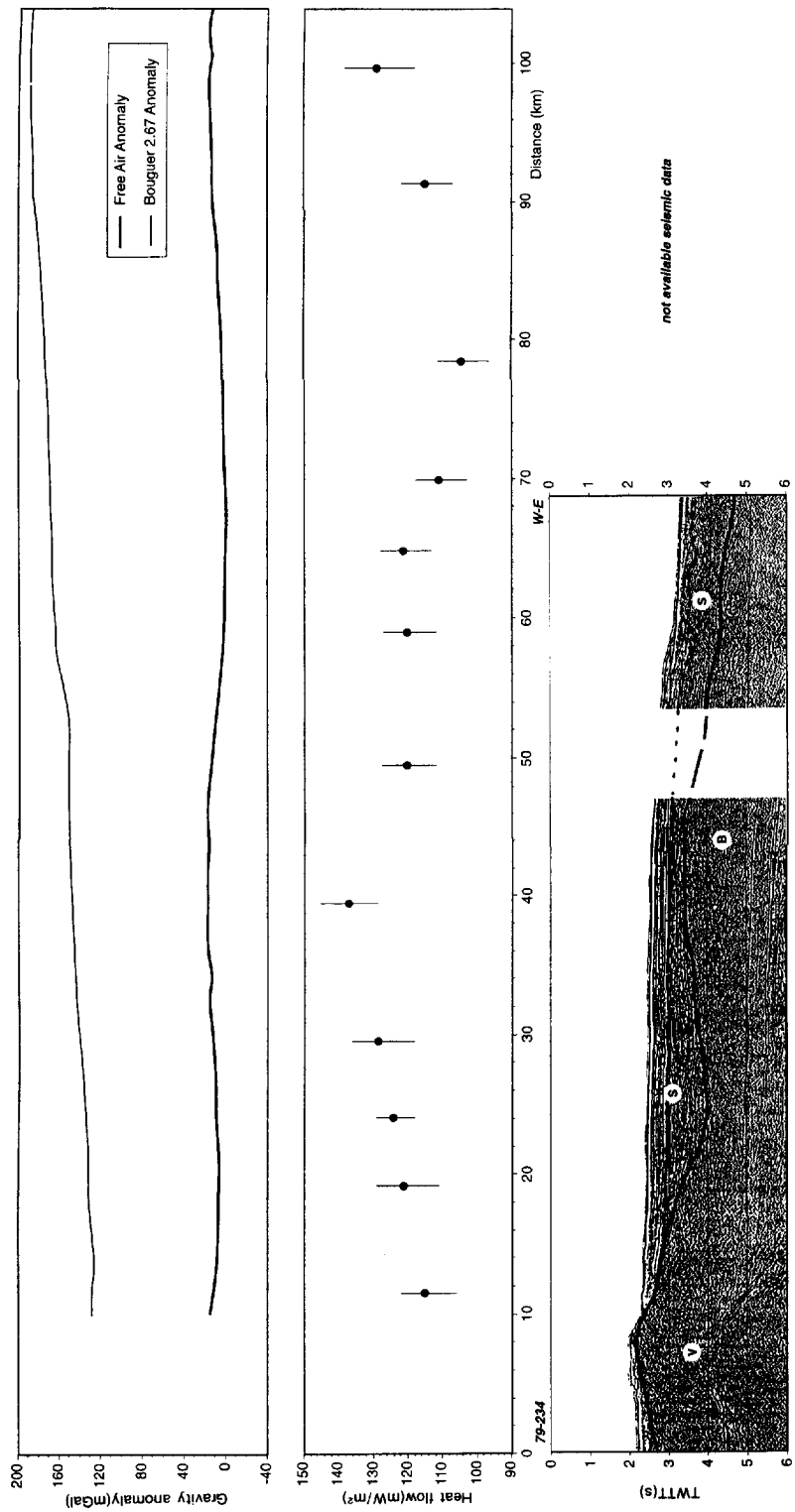

Fig. 10. Composed heat flow, gravity and seismic profile corresponding to the EAB-1 and EAB-2 heat flow trajects (Fig. 3). S = Neogene–Quaternary sedimentary cover; B = acoustic basement; V = volcanics. Dotted line indicates the Miocene–Pliocene limit.

in age, presents a wide variation in thickness reaching maximum values of 5–6 km in the southern and northern WAB. For this layer we have assumed an intermediate thermal conductivity value of 2.0 $W m^{-1} K^{-1}$ according to Fernàndez et al. (1995) and considering that sediments are overpressured (Jurado and Comas, 1992). The acoustic basement is mainly made up by metamorphic rocks belonging to the different units of the Alboran Crustal Domain. We have assigned to this layer the highest thermal conductivity 3.0 $W m^{-1} K^{-1}$ (ITGE, 1993).

The base of the model is placed at 35 km depth where a constant heat flow of 80 $mW m^{-2}$ have been imposed which corresponds to the average heat flow measured along the modelled profile. At the top of the model, the temperature has been fixed at 12°C according to the measured bottom water temperature. There is no horizontal heat flow across the lateral boundaries of the model.

The corrected heat flow values along the profile show smoother variations than those observed in the measured values (Fig. 11). In particular, the local anomaly situated at the northern edge of the basement high is reduced by the factor of 10–15%. In contrast, the values located at the ends of the profile are increased by a factor of about 10%. Additional corrections to the background heat flow can arise from differences in heat production between the sediments and the basement. However, assuming a maximum heat production contrast of 1 $\mu W m^{-3}$, the resulting corrected heat flow would increase only by to 5–9 $mW m^{-2}$ above the maximum depocentres.

5.2. Transient corrections

According to the geological framework of the Alboran Sea, the major transient shallow effects to

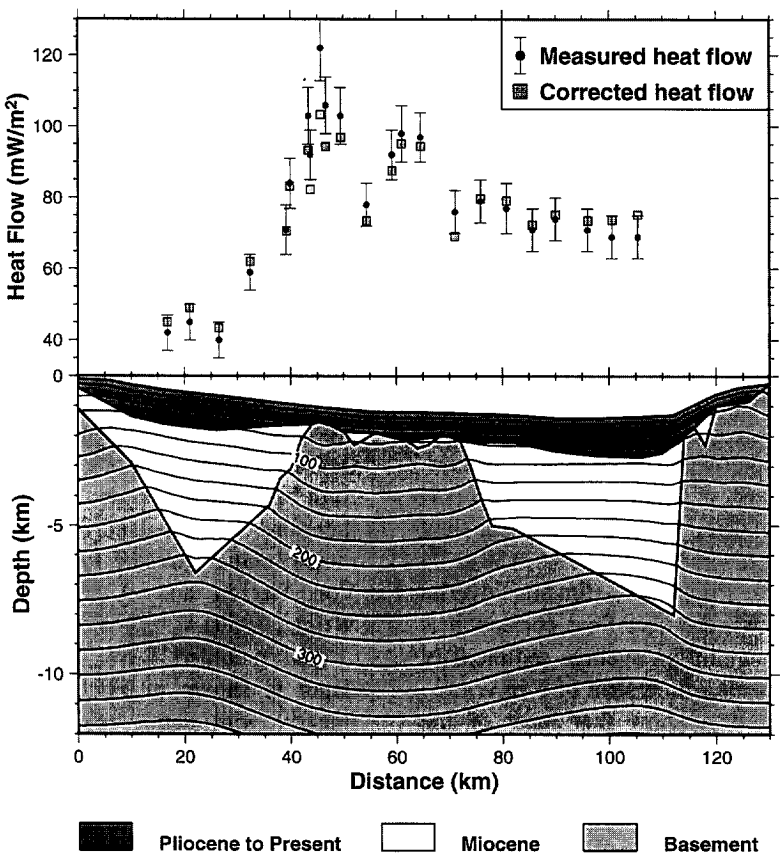

Fig. 11. Effects of steady-state correction on the measured heat flow values corresponding to the WAB-1 heat flow traject.

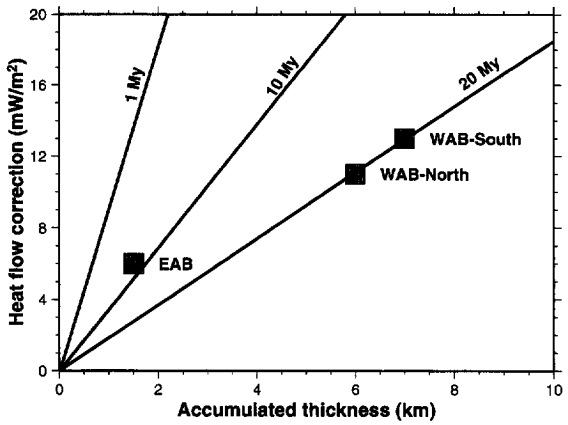

Fig. 12. Heat flow correction associated with sedimentation effects for different sedimentary thicknesses and times.

consider must be sedimentation rate and cooling of volcanic rocks. Heat flow corrections due to sedimentation will be especially noticeable in the WAB where Miocene–Quaternary sedimentary infill of up to 7 km thickness occurs (Fig. 7 and Fig. 11). A rough estimate of this effect may be obtained by solving the heat transport equation in a moving medium for which a 1-D analytical solution is given by Jaeger (1965). The sedimentation effect on the measured heat flow for different duration times of the process are shown in Fig. 12. A constant sedimentation rate without compaction effects has been considered. Therefore, in the WAB, where sediments range from the Burdigalian to Recent (20 m.y. time span), the heat flow correction would be up to 13 $mW\,m^{-2}$ in the southern part (maximum accumulated thickness of 7 km), whereas in its northern part (up to 6 km of accumulated thickness) the heat flow correction would reach a maximum of 11 $mW\,m^{-2}$. In the EAB, where Pliocene sediments overlie Miocene volcanic rocks, the heat flow correction is about 6 $mW\,m^{-2}$ assuming an average sedimentary thickness of 1.5 km with a time span of 5 m.y.

Seismic reflection data show that most of the acoustic basement in the EAB is made up of Miocene interlayered volcanic rocks, although the thickness of this volcanic layer is not well known (see Fig. 10). The volcanic activity occurred from the Serravalian to the Messinian (Hernandez et al., 1987). The measured heat flow in the EAB is fairly constant and exceeds 110 $mW\,m^{-2}$, thus pointing to a possible relationship between volcanic activity and heat flow. In order to maximize the role of volcanism we have calculated the cooling effect of an infinite volcanic sill (e.g., Buntebarth, 1984) with a thickness of 5 km, overlain by a 1.5 km thick sedimentary sequence, and with an age and temperature of intrusion of 5 Ma and 1200°C, respectively. Under these conditions, the cooling effect of the considered sill would be only of 4–5 $mW\,m^{-2}$. Thus, the superposition of the cooling and sedimentation effects tend to neutralize each other.

5.3. Bottom water temperature

The steady-state and transient corrections described above tend to smooth inequally the heat flow values obtained at the entire Alboran Basin. The heat flow in the EAB would remain unmodified with an average value of 121–126 $mW\,m^{-2}$. In the WAB, the values located at the basement high will be reduced by about 5–10 $mW\,m^{-2}$, whereas those located above the maximum Miocene depocentres could increase by 15–20 $mW\,m^{-2}$, thus smoothing the centrewards increase of the measured heat flow. However, the resulting heat flow in the northern and westernmost WAB remains anomalously low, whereas in the southwesternmost part it results in a relative high. All these "anomalous" values are close to the shoreline and the Gibraltar Strait where deeply penetrating mesoscale oceanic eddies could produce variations in the bottom water temperature (BWT). These variations cause a thermal disequilibrium between sediments and sea bottom water, and, therefore, the measured thermal gradient is overestimated/underestimated for cold/warm streams (e.g., Von Herzen and Anderson, 1972; Louden and Wright, 1989).

The recorded BWT at each site versus water depth is shown in Fig. 13a. The BWT increases linearly with depth below 1000 m with a fairly constant gradient of about 0.15 $mK\,m^{-1}$. Above this depth — i.e., sites close to the shoreline — the BWT-depth plot shows a bimodal distribution in which one of the branches follows the previous trend whereas the other shows a reversed one. A striking

feature is that branch A (BWT increasing with water depth) encompasses the heat flow sites located in the southwestern WAB, while branch B comprises those sites located at the northern part of the Alboran Sea (WAB and DB). At first sight, it would appear that branch A is a continuation of the deep trend. How-

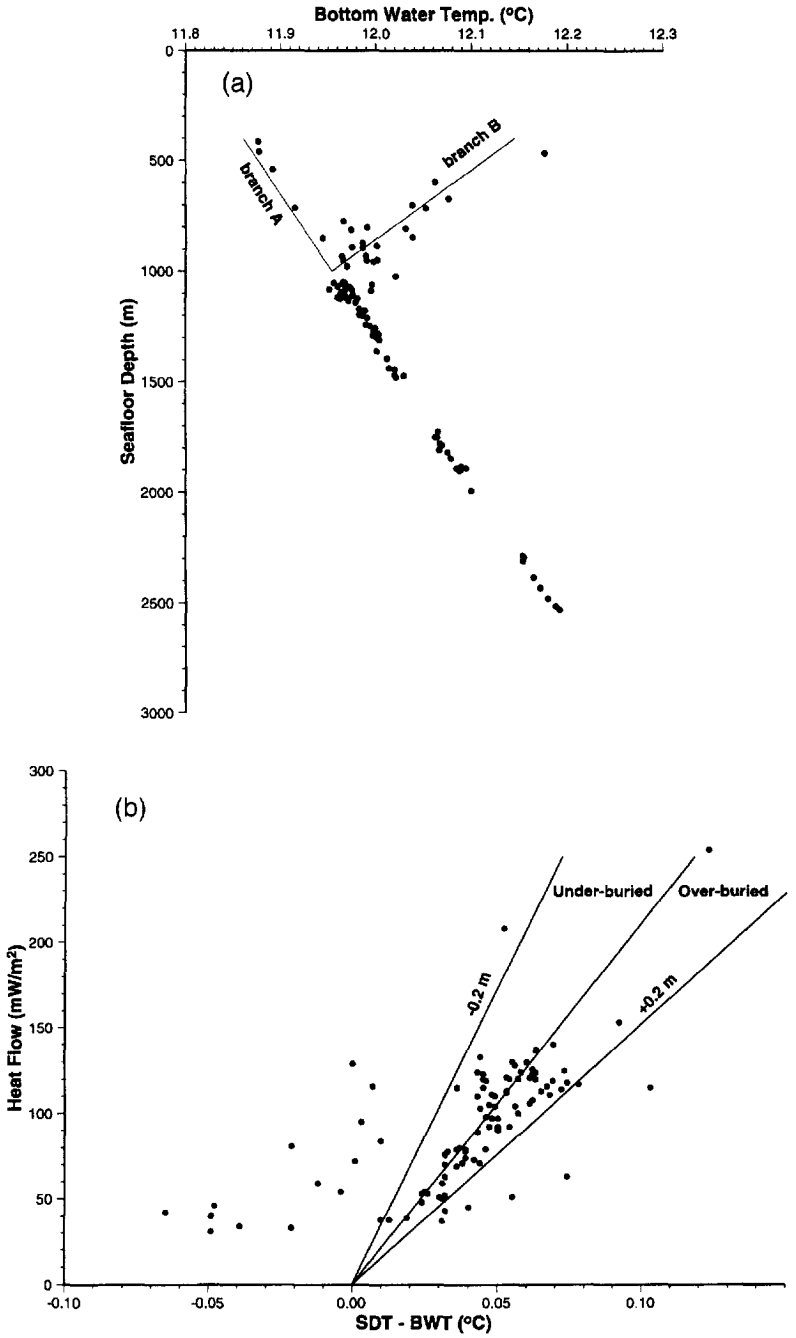

Fig. 13. (a) Variation in bottom water temperature vs. sea floor depth. (b) Temperature difference between sediments (*SDT*) and bottom water (*BWT*) vs. measured heat flow.

ever, as will be shown in the following, neither of these two branches is representative of the shallower bottom water temperature trend.

To determine whether the northern Alboran Sea is affected by cold deep oceanic eddies and the southwestern WAB is anomalously warm, or if both are influenced by deep eddies, we have plotted the measured heat flow against the temperature difference between the uppermost sediments (temperature measured at the upper G-line sensor, SDT) and the sea bottom water (Fig. 13b). Assuming constant thermal conductivity and bottom water temperature, all the points should follow a straight line which, in turn, is related to the penetration depth of the probe. In our case, the linear regression applied to the main population, when a thermal conductivity of 1.26 $W m^{-1} K^{-1}$ is considered, shows an average penetration depth for the uppermost sensor of about 0.6 m. As the penetration depth of the probe is not known, we have considered a variation of ± 0.2 m in this parameter. In Fig. 13b is shown that most of the sites fall within this interval, except a few of them which are completely out of range because of thermal disequilibrium between the sediments and the sea bottom water. From this analysis we conclude that the BWT in those sites located in the northwestern WAB (#4, 5, 6, 7, 9, 10, 46, 47, 48 and 63) is anomalously high. In contrast, the BWT corresponding to the southwestern sites in the WAB (#31, 32, 33 and 34) is anomalously low. BWT variations are probably related to influx of deep cold water from the Atlantic Ocean into the southwesternmost WAB and deep outflow of warmer Mediterranean water through its northern part (Lacombe et al., 1972).

Considering the temperature difference between the sediments and sea bottom water, we conclude that the heat flow measured in the northwestern WAB is highly underestimated while in the southwestern WAB it is slightly overestimated. A better knowledge of the behaviour of the Atlantic–Mediterranean streams, their temperature fluctuation and periodicity, if any, could help to quantify better the heat flow correction associated with this effect.

6. Discussion

In the previous section we have estimated the order of magnitude of the heat flow corrections applicable to the Alboran Sea heat flow measurements. These corrections would increase the measured heat flow along the borders of the WAB where very thick Miocene and Pliocene sedimentary sequences are present. Furthermore, the thermal refraction correction tends to decrease the local thermal anomalies observed at the basement highs. In the EAB, the corrected heat flow does not differ substantially from the measured one. The resulting heat flow pattern in the Alboran Basin is therefore smoother than the uncorrected one, although the increase towards the centre clearly persists. Likewise, the corrected heat flow shows an increasing trend from the west (Gibraltar Strait) to the east (Alboran Ridge) in the WAB, from where it is roughly constant throughout the EAB.

To obtain a first-order estimate of the lithospheric thermal structure in the Alboran Sea, a 1-D approach which combines surface heat flow and bathymetry data has been applied (Lachenbruch and Morgan, 1990). This approach assumes local isostasy and compares the buoyancy of a given lithospheric column with that from the mid-oceanic ridges where its thickness, mean density and buoyancy are known. In this way, elevation depends on the mean density and thickness of both the crust and the lithospheric mantle. The density of the lithospheric mantle is assumed to be temperature dependent — i.e., it is the same as that of the asthenosphere but corrected for thermal expansion. Therefore, elevation is given by (Lachenbruch and Morgan, 1990):

$$\epsilon = \frac{\rho_a - \rho_l}{\rho_a} L - H_0 \qquad \text{for } \epsilon > 0$$

$$\epsilon = \frac{\rho_a}{\rho_a - \rho_w}\left(\frac{\rho_a - \rho_l}{\rho_a} L - H_0\right) \qquad \text{for } \epsilon < 0$$

where ϵ = elevation above sea level (m), ρ_a = density of the asthenosphere (3200 $kg m^{-3}$), ρ_l = mean density of the lithosphere ($kg m^{-3}$), ρ_w = density of sea water (1000 $kg m^{-3}$), L = lithospheric thickness (m) and H_0 = depth below sea level of an unloaded asthenospheric column (2400 m).

The density of the lithospheric mantle is given by Lachenbruch and Morgan, 1990:

$$\rho_m(z) = \rho_a\{1 + \alpha[T_a - T(z)]\}$$

where $\rho_m(z)$ = density of the lithospheric mantle at a depth "z" (kg m^{-3}), α = thermal expansion coefficient ($3.5 * 10^{-5}$ K^{-1}), T_a = temperature at the lithosphere–asthenosphere boundary (1350°C) and $T(z)$ = temperature of the lithospheric mantle at a depth "z" (°C).

The temperature–depth distribution and thus the mantle density for any lithospheric column are given by the surface heat flow, once the crustal thickness (including the sediments, and the upper and lower crust) and heat production distribution are fixed (e.g., Cabal and Fernàndez, 1995). Therefore, the elevation will be determined by the surface heat flow and by the mean density and thickness of the crust, provided that the lithospheric mantle thickness is given by the 1350°C isotherm.

The depth of the Moho in the Alboran Sea is not very well determined because deep seismic data are scarce and of insufficient quality. Recent studies that combine seismic and gravity data show that the Moho depth could range between 15 and 22 km (Torné and Banda, 1992; Watts et al., 1993). Because of these uncertainties, a parametric analysis to estimate the range of possible crust and lithosphere thicknesses compatible with the observed heat flow and water depth in the WAB was made (Fig. 14a). The adopted values for density, thermal conductivity and heat production are summarized in Table 4. As average, we have assumed that a 5 km thick sedimentary layer is covering the whole WAB. With such thickness, the modelling results will be highly sensitive to the adopted density for the sediments. In fact, a variation of 100 kg m^{-3} is equivalent to 230 m in elevation.

From the obtained results, it can be inferred that the total crustal thickness (including the water column) in the WAB may vary from a maximum of 21 km for a water depth of 800 m and a heat flow of 70 mW m^{-2}, to a minimum of about 13 km for a bathymetry of 1300 m and a heat flow of 105 mW m^{-2}. Note that a crustal thickness less than 15 km in the central part of the WAB is not consistent with a heat flow lower than 80 mW m^{-2} even when considering a low density for sediments of 2300 kg m^{-3}. The resulting lithospheric thickness in the WAB decreases towards the centre from about 90 km near the boundaries, if we assume a corrected heat flow of 70 mW m^{-2} in this area, to about 50 km in the central and eastern parts where the maximum heat flow is reached (Fig. 14b).

In the EAB, the most striking feature is that, while the heat flow appears to be roughly constant, the water depth increases towards the east from about 1000 m in the SAB to more than 2500 in the eastern EAB. Assuming local isostasy, this suggests that either the crustal density is increasing, or the crustal thickness is decreasing towards the east, or a combination of both. The range of crustal thickness which is compatible with the observed bathymetry for a surface heat flow of 115 and 125 mW m^{-2} is shown in Fig. 15. For a heat flow of 115 mW m^{-2}, the maximum crustal thickness would be around 15 km in the SAB, whereas in the eastern EAB it would reach a maximum of 11.5 km.

In principle, we have assumed a crustal density of 2800 kg m^{-3} (without sediments) and a 1.5 km thick Pliocene sedimentary layer with a density of 2200 kg m^{-3} (Table 4). To maximize the average crustal density, we have considered an increase of 50 kg m^{-3} in the subsediment crust and a decrease in the thick-

Table 4
Values used in the heat flow, crustal structure and elevation parametric study

	West Alboran Basin			East Alboran Basin		
	Density [a]	Th. conductivity	Heat production [a]	Density [a]	Th. conductivity	Heat production [a]
	(kg m^{-3})	(W m^{-1} K^{-1})	(μW m^{-3})	(kg m^{-3})	(W m^{-1} K^{-1})	(μW m^{-3})
Sediments	2300–2400	2.0	1.0	2200	2.0	1.0
Crust	2800	3.0	$2.0 \exp(-z/15{,}000)$	2800–2850	2.5	$2.0 \exp(-z/15{,}000)$
Lith. Mantle	[b]	3.4	0.0	[b]	3.4	0.0

[a] Density values come from Torné and Banda (1992) and Watts et al. (1993). Heat production for sediments and crust come from Cabal (1993). Other parameters are from Zeyen and Fernàndez (1994).

[b] Lithospheric mantle density is temperature dependent, being equal to $3200\{1 + 3.5 * 10^{-5}[T_a - T(_z)]\}$ and T_a = 1350°C.

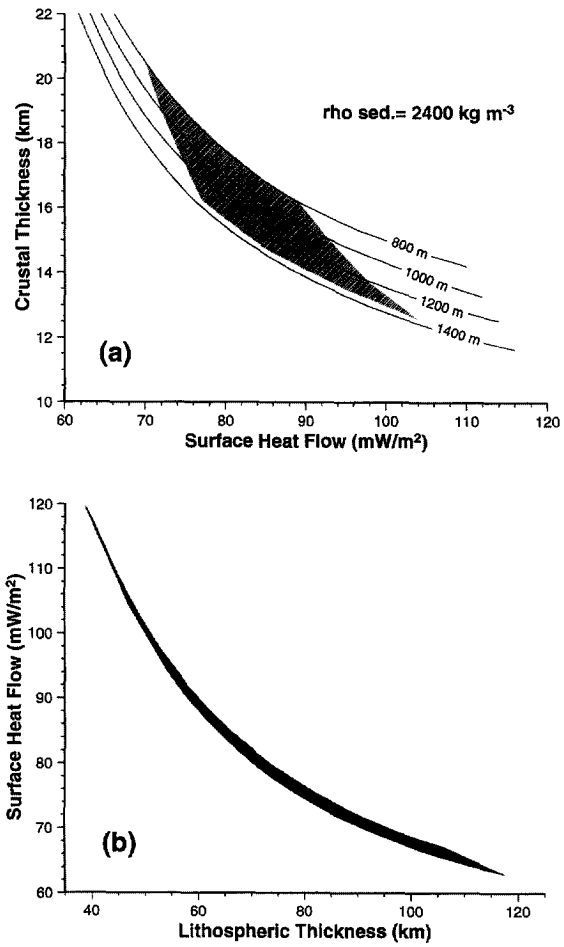

Fig. 14. Results of the parametric study carried out for the West Alboran Basin where a 5 km thick sedimentary layer has been considered. (a) Variation in crustal thickness vs. surface heat flow for different water depths. Shaded area indicates the range of possible crustal thickness values in the West Alboran Basin. (b) Variation in lithospheric thickness vs. surface heat flow.

ness of the sedimentary layer of 0.5 km. These variations in the crustal density and sedimentary thickness can be argued by the eastward increase in the amount of volcanic bodies forming the acoustic basement of the Alboran Basin, and by the lateral thinning of the sedimentary sequence observed towards the residual volcanic highs (Fig. 10). As a result, the total lithospheric thickness in the EAB is maintained constant around 35–40 km for a surface heat flow of 115–125 mW m^{-2}.

The obtained crustal thickness in the eastern EAB is noticeably less than that proposed by Torné and Banda (1992) and Watts et al. (1993). Torné and Banda (1992), in a gravity profile that ends up in our modelled area, suggested that the total crustal thickness has a minimum value of about 15 km, whereas Watts et al. (1993), in a gravity model that crosses the entire basin, have found values between 16 and 19 km in the central part of the basin. The minimum values proposed by these authors correspond to the assumption of a low-density uppermost mantle as proposed by Hatzfeld (1976). However, such anomalous mantle would result, in our modelling, in an even lower crustal thickness. This discrepancy is explained by the influence on the gravity model of the dramatic lithosphere thinning that is now evident from the heat flow data and that was not taken into account in the previous studies.

The local thermal anomalies encountered in the central part of the WAB, DB and SAB, can be attributed to hydrothermal activity related with recent normal faults or residual volcanic highs. In the central WAB these anomalies are probably related to forced convection with the Betics being the recharge area, and the deep low-angle faults associated with the basement high acting as an ascent conduit. A similar mechanism has been described by Fernàndez and Banda (1990) to explain onshore local thermal anomalies associated with master faults. Offshore thermal anomalies produced by groundwater circulation with the recharge area inland have been also described in the northwestern border of the Valencia Trough (Fernàndez et al., 1990). A similar mechanism is proposed for the anomalies located in the SAB where a NE–SW-directed fault system with recent strike-slip movement is present.

The Djibouti Bank thermal anomaly, with its highest for the Alboran Sea heat flow value (up to 254 mW m^{-2}), is located very close to a residual volcanic high. Provided that the heat released by a magmatic body associated with this volcano, presumably of pre-Pliocene age, is not enough to produce such anomaly, the driving mechanism could be related to forced convection. In this case, the discharge area could be associated with high permeability of volcanic rocks rather than with deep faults. A better understanding of the origin of these local thermal anomalies needs complementary studies which are beyond the scope of this paper.

The Alboran Basin, like other Mediterranean

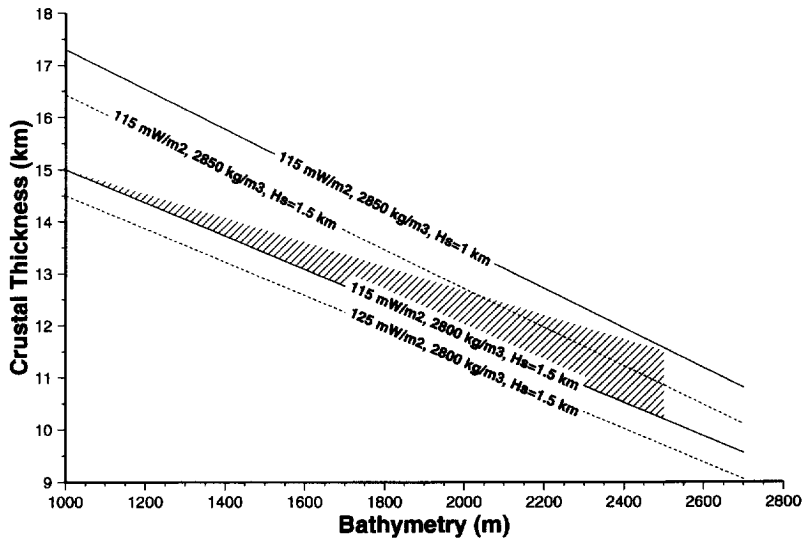

Fig. 15. Variation in crustal thickness vs. bathymetry for different values of crustal density, surface heat flow and sedimentary thickness in the East Alboran Basin. Shaded area indicates the range of possible crustal thickness values in the East Alboran Basin.

basins, such as the Tyrrhenian, Pannonian and Aegean basins, is underlain by a thin continental or, in some places, oceanic crust, and a thin lithosphere (e.g., Malinverno and Ryan, 1986). These mediterranean-type back-arc basins, also called as marginal or internal basins, are located on the concave side of arucate mountain belts and are characterized by a high heat flow and recent (Miocene to Quaternary) volcanic activity and fast subsidence. These similarities are particularly relevant to the western margin to 10 km in the central part of the basin, where the water depth exceeds 3000 m. The measured heat flow ranges there from 134 to 150 $mW\,m^{-2}$, with local values of up to 300 $mW\,m^{-2}$ (Erickson et al., 1977; Della Vedova et al., 1984; Hutchison et al., 1985; Khutorskoy et al., 1986).

7. Concluding remarks

The data acquired during the FLUCALB project have improved significantly the knowledge of the geophysical characteristics of the Alboran Sea. These data include: (a) 98 heat flow determinations in the whole Alboran Sea, the sites covering a water depth interval between 466 and 2530 m; (b) 697 nautic miles of gravity profiles; (c) 1446 nautic miles of bathymetric survey including multi-beam and echo sounder profiles; and (d) 22 gravity cores covering the water depth range from 403 to 2236 m.

The measured heat flow shows remarkable differences between the western and eastern parts of the Alboran Basin. The average heat flow in the WAB is 69 ± 6 $mW\,m^{-2}$, with a generally increasing trend towards the centre and to the east. In the contrast, the heat flow pattern in the EAB shows a high average value of 124 ± 8 $mW\,m^{-2}$ which is rather constant over the area. Superimposed on this general pattern are some local thermal anomalies, most probably associated with hydrothermal activity, which have been detected in the central WAB (up to 123 $mW\,m^{-2}$), the SAB (up to 153 $mW\,m^{-2}$) and in the DB (up to 254 $mW\,m^{-2}$). After corrections for thermal refraction, sedimentation rate and cooling of volcanic bodies the variation in the resulting heat flow in the WAB is smoother, but still shows the increasing trend towards the centre and to the east. In the EAB, application of these corrections do not produce noticeable changes.

The obtained heat flow values agree, in general, with previous heat flow determinations except in the EAB, where the only available measurement indicates a value of 33 $mW\,m^{-2}$ (Fig. 1). This value has to be ruled out as being indicative of the regional

thermal regime in the EAB in the light of the number and consistency of the new measurements. Furthermore, the resulting heat flow pattern in the Alboran Sea shows some differences with that drawn in the Heat Flow Map of Europe (Cermak and Hurtig, 1979) where, due to the scarcity of data, a minimum value of 60 $mW\,m^{-2}$ was proposed for most of the EAB.

A careful analysis of the bottom water temperature versus depth for depths less than 1 km, and of the temperature of the uppermost sediments indicates that deep water streams can perturb the sea floor thermal gradient in the proximity of the Gibraltar Strait. Cold water inflow from the Atlantic Ocean affects the southwestern WAB, while warm water from the Mediterranean produces the opposite effect in the north-northwestern WAB.

A 1-D modelling approach that combines heat flow data, crustal structure and elevation, shows a remarkable lithospheric thinning from the WAB, where it ranges between 90 and 50 km, to the EAB where it is about 35–40 km only. This change is even more spectacular in the N–S direction, provided that under the Iberian Peninsula and the African plate, the lithospheric thickness could reach values higher than 100–120 km (Zeyen and Fernàndez, 1994; Torné et al., 1995). Based on this approach, it is inferred that the crustal thickness should be, in average, of 14–16 km in the central part of the WAB increasing towards the borders of the basin. In the EAB, the crustal thickness may vary between 12.5 and 14.5 km in the western EAB, and between 10 and 11.5 km in the eastern EAB. The thermal anomalies encountered near the Alboran Ridge do not allow estimating how the crustal thickness evolves over the transition from the WAB to the EAB.

These results put primary constraints on models of the Alboran Sea formation. Therefore, any of the genetic hypotheses mentioned in the introduction must be consistent with the heat flow pattern presented in this paper and with the inferred crustal and lithospheric structure. Our present-day knowledge about the geodynamics of the Alboran Sea is still far from complete to allow proposing a self-consistent model. However, further developments in modelling and data acquisition, especially in the North Algerian–South Balearic Basin, will add important information and knowledge towards a better understanding of the evolution of this region.

Acknowledgements

This work has been carried out with the financial support of the Ministry of Science and Technical Policy of Russia, the Ministry of Education and Science of Spain (CICYT, AMB-94-1113-E; DGICYT, PB-91-0080-C0201), the European Union (Integrated Basin Studies, JOU2-CT92-110), the Department of Marine Expedition Work of the Russian Academy of Sciences, and the Russian Foundation for Fundamental Research (grant N 93-14086). We acknowledge the participation of the following institutions: Scientific Industrial Center "Tekhnologia" (Samara), Saratov State University (Saratov) and University of Meknes (Morocco). We also are indebted to engineers N.D. Kalinin, S.N. Malykhin, O.A. Lipatov, V.P. Turkov, B.I. Yepikhin and V.K. Pigarin, and to the Captain L.V. Sazonov and the crew of the R/V "Akademik Nikolaj Strakhov". We thank Carmel Lowe and Stefan Bachu for their thorough reviews of the manuscript.

References

Albert-Beltran, J.F., 1979. Heat flow and temperature gradient data from Spain. In: V. Cermak and L. Rybach (Editors), Terrestrial Heat Flow in Europe. Springer, Berlin–Heidelberg, pp. 261–266.

Allan, T.D. and Morelli, C., 1971. A geophysical study of the Mediterranean. Boll. Geofis. Teor. Appl., 13: 99–142.

Balanyá, J.C. and García-Dueñas, V., 1987. Les directions structurales dans le Domain d'Alboran de part et d'autre du D'etroit de Gibraltar. C. R. Acad. Sci. Paris, 304: 929–933.

Banda, E. and Ansorge, J., 1980. Crustal structure under the central and eastern part of the Betic Cordillera. Geophys. J. R. Astron. Soc., 63: 515–532.

Bonini, W.E., Loomis, T.P. and Robertson, J.D., 1973. Gravity anomalies, ultramafic intrusions and the tectonic of the region around the Straits of Gibraltar. J. Geophys. Res., 78: 1372–1382.

Buntebarth, G., 1984. Geothermics. An Introduction. Springer, Berlin, 144 pp.

Cabal, J., 1993. Régimen térmico en el noroeste de la Península Ibérica y sus márgenes continentales: flujo de calor, producción radiogénica de calor y estructura térmica de la litosfrea. Ph.D. Thesis, Univ. Oviedo, 186 pp.

Cabal, J. and Fernàndez, M., 1995. Heat flow and regional uplift at the northeastern border of the Ebro basin (NE-Spain). Geophys. J. Int., 121: 393–403.

Cermak, V. and Hurtig, E., 1979. Heat flow map of Europe. In: V. Cermak and L. Rybach (Editors), Terrestrial Heat Flow in Europe. Springer, Berlin–Heidelberg, p. 36.

Channel, J.E.T. and Mareschal, J.C., 1989. Delamination and asymmetric lithospheric thickening in the development of the Tyrrhenian Rift. In: M. Coward, D. Dietrich and R.G. Park (Editors), Alpine Tectonics. Geol. Soc. London, Spec. Publ., 45: 285–300.

Comas, M.C., García-Dueñas, V. and Jurado, M.J., 1992. Neogene tectonic evolution of the Alboran Basin from MCS data. Geo-Mar. Lett., 12: 157–164.

Comas, M.C., García-Dueñas, V., Soto, J.I. and Campos, J., 1993. An extensional basin developed on a collisional orogen: The Alboran Sea. In: M. Seranne and J. Malavieille (Editors), Late Orogenic Extension in Mountain Belts. BRGM Geol. Min. Doc., 219: 44–46.Structure and evidences for extension in the Alboran Sea basin: implications for tectonic evolution. Tectonics (in press).

Della Vedova, B., Pellis, G., Foucher, J.P. and Rehault, J.P., 1984. Geothermal structure of the Tyrrhenian Sea. Mar. Geol., 55: 271–289.

Dercourt, J., Zonenshain, L.P. and Ricou, L.E., 1986. Geological evolution of the Tethys belt from the Atlantic to the Pamirs since the Lias. Tectonophysics, 123: 241–315.

Dewey, J.F., Helman, M.L., Turco, E., Hutton, D.H.W. and Knott, S.D., 1989. Kinematics of the western Mediterranean. In: M. Coward (Editor), Alpine Tectonics. Geol. Soc. London, Spec. Publ., 45: 265–283.

Erickson, A.J., Simmons, G. and Ryan, W.B.F., 1977. Review of heat flow data from the Mediterranean and Aegean seas. In: B. Biju-Duval and L. Montadert (Editors), Int. Symp. on the Structural History of the Mediterranean Basins. Technip, Paris, pp. 263–279.

Fernàndez, M. and Banda, E., 1990. Geothermal anomalies in the Vallés-Penedés graben master fault: convection through the horst as a possible mechanism. J. Geophys. Res., 95: 4887–4894.

Fernàndez, M., Torné, M. and Zeyen, H., 1990. Modelling of thermal anomalies in the NW border of the Valencia Trough by ground-water convection. Geophys. Res. Lett., 17: 105–108.

Fernàndez, M., Foucher, J.P. and Jurado, M.J., 1995. Evidence for the multi-stage formation of the south-western Valencia Trough. Mar. Pet. Geol., 12: 101–109.

Galdeano, A. and Rossignol, J.C., 1977. Assemblage à altitude constante des cartes d'anomalies magnétiques couvrant l'ensamble du bassin occidental de la Méditerranée. Bull. Soc. Géol. Fr., 7: 461–468.

García-Dueñas, V., Balanyá, J.C. and Martínez-Martínez, J.M., 1992. Miocene extensional detachments in the outcropping basement of the northern Alboran basin (betics) and their tectonic implications. Geo-Mar. Lett., 12: 88–95.

Haenel R., 1979. A critical review of heat flow measurements in sea and lake bottom sediments. In: V. Cermak and L. Rybach (Editors), Terrestrial Heat Flow in Europe. Springer, Berlin–Heidelberg, pp. 49–73.

Hatzfeld, D., 1976. Etude seismologique et gravimétrique de la structure profonde de la mer d'Alboran: mise en évidence d'un manteau anormal. C. R. Acad. Sci. Paris, 283: 1021–1024.

Hatzfeld, D. and The Working Group for Deep Seismic Sounding, 1978. Crustal seismic profiles in the Alboran Sea — Preliminary results. Pure Appl. Geophys., 116: 167–180.

Hernandez, J., De Larouzière, F.D., Bolze, J. and Bordet, P., 1987. Le magmatisme néogène bético-rifain et le couloir de décrochement trans-Alboran. Bull. Soc. Geol. Fr., 3: 257–267.

Horvath, F. and Berckhemer, H., 1982. Mediterranean backarc basins. In: H. Berckhemer and K. Hsü (Editors), Alpine Mediterranean Geodynamics. Am. Geophys. Union, Washington, DC, pp. 141–174.

Hutchison, I., Von Herzen, R.P., Louden, K.E., Sclater, J.G. and Jemsek, J., 1985. Heat flow in the Balearic and Tyrrhenian Basins, Western Mediterranean. J. Geophys. Res., 90: 685–701.

ITGE, 1993. Trabajos de medición e inventario de datos de flujo de calor en España: Cordilleras Béticas y suroeste peninsular. Inst. Geol. Miner. España, Madrid, 64 pp.

Jaeger, J.C., 1965. Application of the theory of heat conduction to geothermal measurements. In: W.H.K. Lee (Editor), Terrestrial Heat Flow. Am. Geophys. Union, Geophys. Monogr., 8: 7–23.

Jurado, M.J. and Comas, M.C., 1992. Well log interpretation and seismic character of the Cenozoic sequence in the North Alboran Sea. Geo-Mar. Lett., 12: 129–136.

Khutorskoy, M.D., Gorodnitsky, A.M., Golmstock, A.Ya., Sochelnikov, V.V. and Kondyurin, A.V., 1986. Heat flow, basaltic volcanism and lithosphere structure of the Tyrrhenian Sea. Geotektonika, 5: 116–123 (in Russian).

Khutorskoy, M.D., Fernandez, R., Kononov, V.I., Polyak B.G., Matveev, V.G. and Rot, A.A., 1990. Heat flow through the sea bottom around the Yucatan Peninsula. J. Geophys. Res., 95: 1223–1237.

Lachenbruch, A.H. and Morgan, P., 1990. Continental extension, magmatism and elevation. Formal relations and rules of thumb. Tectonophysics, 174: 39–62.

Lacombe, H., Tchernia, P. and Gamberoni, L., 1972. Variable bottom water in the western Mediterranean Basin. Prog. Oceanogr., 14: 319–338.

Louden, K.E. and Wright, J.A., 1989. Marine heat flow data: A new compilation of observations and brief review of its analysis. In: J.A. Wright and K.E. Louden (Editors), Handbook of Seafloor Heat Flow. CRC Press, Boca Raton, FL, pp. 3–70.

Malinverno, A. and Ryan, W.B.F., 1986. Extension in the Tyrrhenian Sea and shortening in the Apennines as result of arc migration driven by sinking of the lithosphere. Tectonics, 5: 227–245.

Matveev, V.G. and Rot, A.A., 1988. New technique for monitoring of marine geothermal researchers on the shelf. In: Yu.M. Puschcharovsky and V.I. Kononov (Editors), Geothermal Researches on Subaqueous Floor. Nauka, Moscow, pp. 98–107 (in Russian).

Morelli, C., 1985. Geophysical contribution to the knowledge of the Mediterranean crust. In: D.J. Stanley and F.C. Wezel (Editors), Geological Evolution of the Mediterranean Basin. Springer, New York, NY, pp. 65–82.

Platt, J.P. and Vissers, R.L.M., 1989. Extensional collapse of thickened continental lithosphere: a working hypothesis for the Alboran Sea and Gibraltar Arc. Geology, 17: 540–543.

Polyak, B.G., Bouysse, Ph., Kononov, V.I., Butuzova, G.Yu., Criaud, A., Dvorov, V.I., Khutorskoy, M.D., Matveev, V.G., Paduchikh, V.I., Radionova, E.P., Rot, A.A., Tolstikhin, I.N., Voznesensky, A.I. and Zverev, V.P., 1992. Evidence of submarine hydrothermal discharge to the northwest of Guadeloupe Island (Lesser Antilles island arc). J. Volcanol. Geotherm. Res., 54: 81–105.

Rehault, J.P., Boillot, G. and Mauffret, A., 1985. The Western Mediterranean basin. In: D.J. Stanley and F.C. Wezel (Editors), Geological Evolution of the Mediterranean Basin. Springer, New York, NY, pp. 101–129.

Ryan, W.B.F., Hsü, K.J., Cita, M.B., Dumitrica, P., Lort, J., Mayne, W., Nesteroff, W.D., Pautot, G., Stauder, H. and Wezel, F.C., 1973. Init. Rep. of Deep Sea Drilling Project. G.P. Off., Washington, DC, pp. 43–89.

Torné, M. and Banda, E., 1992. Crustal thinning from the Betic Cordillera to the Alboran Sea. Geo-Mar. Lett., 12: 76–81.

Torné, M., Fernàndez, M., Carbonell, J. and Banda, E., 1995. Lithospheric transition from continental to oceanic at the West Iberia Atlantic Margin. In: E. Banda, M. Talwani and M. Torné (Editors), Rifted Ocean–Continent Boundaries. Kluwer, Dordrecht, pp. 247–263.

Von Herzen, R.P. and Anderson, R.N., 1972. Implications of heat flow and bottom water temperature in the Eastern Equatorial Pacific. Geophys. J. R. Astron. Soc., 26: 427–458.

Von Herzen, R.P. and Maxwell, A.E., 1959. The measurement of thermal conductivity of deep-sea sediments by a needle probe method. J. Geophys. Res., 64: 1557.

Watts, A.B., Platt, J.P. and Buhl, P., 1993. Tectonic evolution of the Alboran Sea basin. Basin Res., 5: 153–177.

Weijermars, R., 1985. Uplift and subsidence history of the Alboran Basin and a profile of the Alboran Diapir (W-Mediterranean). Geol. Mijnbouw, 64: 349–356.

Zeyen, H. and Fernàndez, M., 1994. Integrated lithospheric modeling combining thermal, gravity and local isostasy analysis: Application to the NE Spanish Geotransect. J. Geophys. Res., 99: 18,089–18,102.